2006

Self referencing SPR sensor by simultaneous excitation of long and short range surface plasmon modes

Raghunandan K. Donipudi
University of Kentucky, Raghu.Donipudi@marlabs.com

Abstract of Thesis

Self referencing SPR sensor by simultaneous excitation of long and short range surface plasmon modes

A novel surface plasmon resonance sensor is fabricated to evaluate its use in biochemical sensing. The sensor can differentiate between bulk refractive index changes and surface binding reactions of interest. There has been a great interest in developing sensors to differentiate biological or chemical agents from interfering effects, but they still remain in research phase. In this work, a prism coupler is used to simultaneously excite both long and short range surface plasmon modes of the sensor. The differing sensitivities of the long and short range modes allow one to distinguish surface binding reactions of interest from refractive index fluctuations**.** In this thesis, we have demonstrated the sensor's self referencing capability by detecting the formation of an octadecanethiol self assembled monolayer while varying solution refractive index.

KEYWORDS: Surface-plasmon, Long Range, Short Range, Self-Referencing, Sensitivity.

Raghunandan K Donipudi

Author's Signature

July 27, 2006

Date

Self referencing SPR sensor by simultaneous excitation of long and short range surface plasmon modes

By

Raghunandan K Donipudi

Dr Todd Hastings

Director of Thesis

Dr YuMing Zhang

Director of Graduate Studies

July 27, 2006

Date

RULES FOR THE USE OF THESES

Unpublished theses submitted for the Master's degree and deposited in the University of Kentucky Library are as a rule open for inspection, but are to be used only with due regard to the rights of the authors. Bibliographical references may be noted, but quotations or summaries of parts may be published only with the permission of the author, and with the usual scholarly acknowledgments.

Extensive copying or publication of the thesis in whole or in part also requires the consent of the Dean of the Graduate School of the University of Kentucky.

A library that borrows this thesis for use by its patrons is expected to secure the signature of each user.

Name Date

THESIS

Raghunandan K Donipudi

The Graduate School

University of Kentucky

2006

Self Referencing SPR sensor by simultaneous excitation of long and short range surface plasmon modes

---

THESIS

A thesis submitted in partial fulfillment of the requirements for the degree of Master of Science in the College of Engineering at the University of Kentucky

By

Raghunandan K Donipudi

Lexington, KY

Director: Dr Todd Hastings, Assistant Professor of Electrical Engineering

Lexington, KY

2006

ACKNOWLEDGEMENTS

Dr.Todd Hastings (Advisor)

Mr. George Spiggle

Committee Members

- Dr. Vijay Singh
- Dr. Daniel Lau

Fellow Lab Members

- Adam W Chamberlain
- Babitha Bommalakunta
- Sandhya Pochiraju
- Vashista de Silva

TABLE OF CONTENTS

ACKNOWLEDGEMENTS……III

LIST OF FILES ……VI

LIST OF TABLES …….. ..VII

LIST OF FIGURES ……VIII

CHAPTER 1 INTRODUCTION ……..1

1.1 SPR Sensor Background……1

1.2 Motivation for Self referencing sensors…….3

1.3 Previous work towards self referencing sensors……4

CHAPTER 2 SENSOR THEORY AND DESIGN. ……..8

2.1.1 Principle of sensor operation……8

2.1.2 Calculating Reflection spectrum…….13

2.1.3 Sensitivity of long and short range SPW modes……22

2.2 Selection of Materials and Refractive Indices …….24

2.3 Initial Sensor Design…….25

CHAPTER 3 SENSOR FABRICATION .. ……27

3.1 Spin coating of Teflon…….27

3.2 Deposition of gold…….28

3.3 Measurement of layer thickness…….29

CHAPTER 4 EXPERIMENTAL SECTION...……..30

4.1 Experimental setup.....30

4.2 Description of Experiment.....32

4.3 Experimental Results…….....36

4.4 Analysis and Discussion……..….....44

CHAPTER 5 CONCLUSIONS AND FURTHER WORK 49

APPENDIX...……..……..51

REFERENCES..... 54

VITA …….56

LIST OF FILES

1. RaghunandanDonipudi_MSThesis.pdf

LIST OF TABLES

Table 4.3.1 Comparison of Long Range surface plasmon mode resonance peaks from experiment and simulation(main experiment) 41

Table 4.3.2 Comparison of Short Range surface plasmon mode resonance peaks from experiment and simulation(main experiment) 41

Table 4.4.1 Comparison of sensitivities (experiment, theoretical, theoretical (corrected)) for bulk refractive index changes and surface binding changes 45

Table 4.4.2 Sensitive parameters of long range and short range modes for bulk refractive index and surface binding changes from linear and non-linear model 48

Table A1 Comparison of real part of refractive index (n), imaginary part of refractive index (k), thickness of sample(d) between VASE ellipsometer and our ellipsometer for 10nm sample 51

Table A2 Comparison of real part of refractive index (n), imaginary part of refractive index (k), thickness of sample(d) between VASE ellipsometer and our ellipsometer for 20nm sample 52

Table A3 Comparison of real part of refractive index (n), imaginary part of refractive index (k), thickness of sample(d) between VASE ellipsometer and our ellipsometer for 30nm sample 52

LIST OF FIGURES

Figure 1.1 Prism coupler configuration used to excite surface plasmon waves. It can be seen that the long range modes extend deeply into the dielectric and the short range modes extend deeply into the metal. 2

Figure 1.2 Biomolecular element bound to the metal. It can be seen that the analyte binding to the metal produces a local increase in refractive index and propagation constant. 3

Figure 2.1.1 Dielectric slab surrounding a metal layer of thickness h 9

Figure 2.1.2 Calculated magnetic field profiles of the long- and short- range surface plasmon modes supported by a 55 nm thick gold film between dielectrics with refractive index of 1.33. The fields of the long-range (symmetric) mode penetrate deeply into the dielectric allowing for sensitive measurement of background index changes. The fields of the short-range (anti-symmetric) mode are concentrated at the metal surface for better detection of surface binding. 12

Figure 2.1.3 Refractive index of Teflon AF in the wavelength range 500-1000nm 12

Figure 2.1.4 Calculated dispersion relations for the long-range (LRSP) and short range (SRSP) surface-plasmon modes of a 55-nm thick gold thin film surrounded by a medium with the refractive index of Teflon-AF. Points of maximum coupling to the surface-plasmon modes are indicated at the intersection of the curves 13

Figure 2.1.5 Prism coupler configuration for simultaneously launching long and short range surface plasmon waves. 14

Figure 2.1.6 Shows the calculation of angle θ_1 at the prism-substrate interface. 17

Figure 2.1.7 Reflection spectrum without analyte – BK7+Teflon-AF+Gold stack. Teflon thickness-500nm and gold thickness-60nm. 20

Figure 2.1.8 Reflection spectrum for three different thickness of gold. BK7+Teflon-AF+gold+ethanol stack. Teflon thickness-500nm and three different thickness of Gold- 50nm(blue curve), 55nm(red curve), 60nm(pink curve) 20

Figure 2.1.9: Reflection spectrum with ethanol solution. Pure ethanol solution(blue curve), Refractive index of ethanol increased by 0.001(red curve). 21

Figure 2.1.10: Enlarged Long Range Reflection spectrum of Figure 2.1.9. Pure ethanol solution(blue curve), Refractive index of ethanol increased by 0.001(red curve). 21

Figure 2.1.11 Enlarged Short Range Reflection spectrum of Figure 2.1.9. Pure ethanol solution(blue curve), Refractive index of ethanol increased by 0.001(red curve). 22

Figure 2.3.1 Reflection spectrum for three different thickness of gold. BK7+Teflon+gold+ethanol stack. Teflon thickness-500nm and for three different thickness of Gold. 50nm(blue curve), 100nm(red curve), 32nm(pink curve) 26

Figure 3.2.1 Electron-beam evaporator(University of Kentucky) used to deposit gold. 28

Figure 4.1.1 Schematic diagram of a self-referencing surface-plasmon resonance sensor. The sensor consists of a thin gold film on a buffer layer that is closely matched to the solution in interest. 30

Figure 4.1.2 Picture of the optical system with major component labeled. 31

Figure 4.2.1 Long Range and Short Range modes in the reflection spectrum(experiment). 35

Figure 4.2.2 Top-Plot of long range resonance wavelength with time. Bottom-Plot of short range resonance wavelength with time. 35

Figure 4.3.1: Sensor response (experiment) to refractive index change by adding ethylene glycol to water 37

Figure 4.3.2 Reflection spectrum at different temperatures of water. Blue curve shows the reflection spectrum when there is no solution present 38

Figure 4.3.3 Long range mode response to temperature of water. water at 80C(red curve), After 1 minute of cooling down of water(pink curve), After 2 minutes of cooling down of water(black curve), After 3 minutes of cooling down of water(green curve), After 5 minutes of cooling down of water(yellow curve). 39

Figure 4.3.4 Short range mode response to temperature of water. water at 80C(red curve), After 1 minute of cooling down of water(pink curve), After 2 minutes of cooling down of water(black curve), After 3 minutes of cooling down of water(green curve), After 5 minutes of cooling down of water(yellow curve). 40

Figure 4.3.5 Reflection spectrum from simulation. BK7+Teflon-AF+Gold+ODT varying concentration of Ethanol. Teflon thickness-500nm, gold thickness-60nm, ODT thickness-2nm 42

Figure 4.3.6 Enlarged Long Range Reflection spectrum of Figure 4.3.5. 100% ethanol without ODT(blue curve), 95% Ethanol+5% Methanol without ODT(red curve), 90% Ethanol+10% Methanol without ODT(pink curve), 100% Ethanol with ODT(black curve), 95% Ethanol+5% Methanol with ODT(yellow curve), 90% Ethanol+10% Methanol with ODT(green curve). 43

Figure 4.3.7 Enlarged Short Range Reflection spectrum of Figure 4.3.5. 100% ethanol without ODT(blue curve), 95% Ethanol+5% Methanol without ODT(red curve), 90% Ethanol+10% Methanol without ODT(pink curve), 100% Ethanol with ODT(black curve), 95% Ethanol+5% Methanol with ODT(yellow curve), 90% Ethanol+10% Methanol with ODT(green curve). 43

Figure 4.4.1 Solution index and average surface layer thickness as a function of time during monolayer formation. The labeled regions indicated the solution flowing and correspond to those in Fig. 4.2.2: (1) EtOH, (2) 95% EtOH + 5% MeOH, and (4) 3.2 mM octadecanethiol (ODT) in EtOH. 47

Figure A1 Left figure shows real part of refractive index(n) and right figure shows imaginary part of refractive index(k) for 10nm sample. 53

Figure A2 Left figure shows real part of refractive index(n) and right figure shows imaginary part of refractive index(k) for 20nm sample. 53

Figure A3 Left figure shows real part of refractive index(n) and right figure shows imaginary part of refractive index(k) for 30nm sample. 53

Chapter 1

Introduction

1.1 SPR Sensor Background

Surface Plasmon Resonance (SPR) sensors are extensively used as optical sensors for the detection of biological and chemical analytes. Due to this, SPR biosensors hold a great potential in fields such as food-safety, environmental protection and medicine [1]. SPR biosensors are also used in the analysis of biomolecular interactions. Hence SPR biosensors are also used in real-time monitoring of biomolecules binding to target molecules on the sensor.

A surface plasmon wave is an electromagnetic wave that propagates along the interface of certain metals and a dielectric. Metals such as gold, silver and copper exhibit negative real permittivity at optical wavelengths. However gold is the most widely used metal for SPR based sensors because of its chemical stability and abundant surface functionalization techniques [2].

Direct excitation of surface plasmons at metal dielectric interface is not possible. The most commonly used method to generate a surface plasmon wave is Kretschmann configuration of attenuated total reflection (ATR). The principle behind total internal reflection is that light incident at the interface between materials of refractive indices n_1 and n_2 (where $n_1 > n_2$) is completely reflected beyond a critical angle theta (θ). Surface plasmon resonance occurs when these two conditions are satisfied:

1. The incident angle must be greater than the critical angle
2. The component of incident light's that is parallel to sensor surface matches with the wave vector of surface plasmon wave.

When this happens, the energy of the incident photon is transferred to surface plasmon wave. Fig 1.1 shows the prism coupler configuration for exciting surface plasmon waves. The prism is used to couple some light to SP wave and reflect some light to an optical photo detector. Since an evanescent electric field extends away from the metal surface into the surrounding dielectric, changes in the optical properties of the dielectric will cause the resonance to shift to a different wavelength.

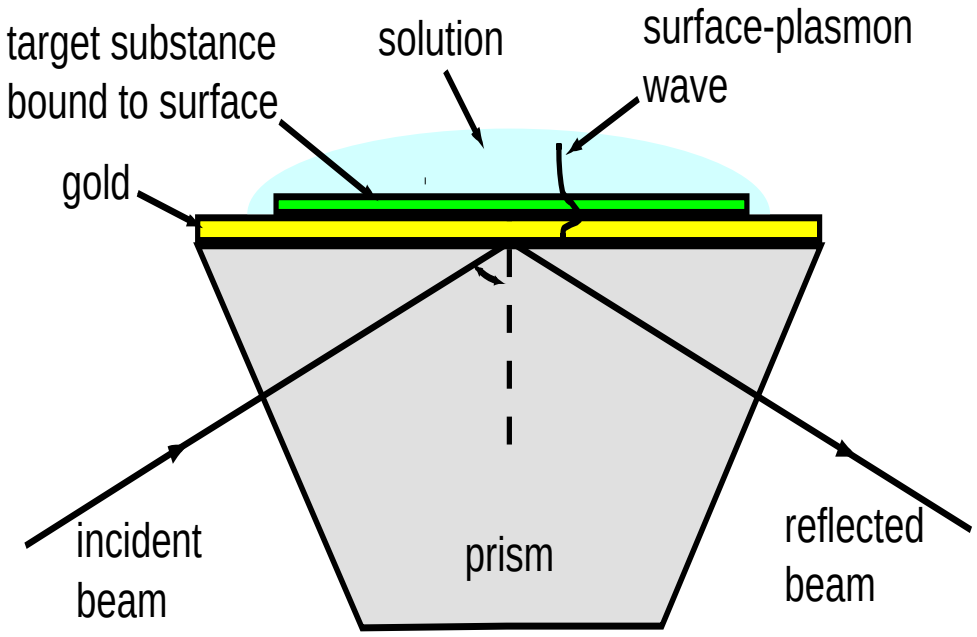

Figure 1.1 Prism coupler configuration used to excite surface plasmon waves

Surface plasmon waves can also be excited by two other systems, grating-couplers and optical waveguides [1]. In this work we limit our explanations to the prism coupler based SPR system, as we used this system in our work.

Concept of surface plasmon resonance biosensing:

Surface plasmon waves are sensitive to changes in the refractive index of dielectric. This is the principle behind SPR biosensors – i.e. binding of a target analyte to immobilzed biomolecular recognition element produces a local increase in refractive index at the sensor surface [1]. This is demonstrated in Fig 1.2. The theory behind surface plasmon resonance sensing will be explained in greater detail in the future sections of this work.

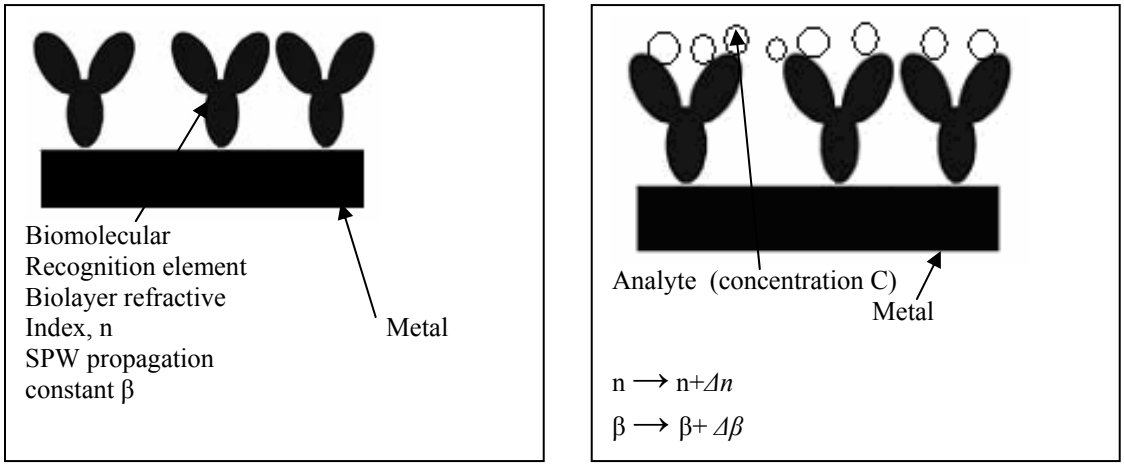

Figure 1.2 The local refractive index near the metal surface changes when the target analyte is flowing through sensor and binds to the biomolecular recognition element.

1.2 Motivation for self-referencing sensors

In general, surface plasmon sensors are sensitive to refractive index variations whether they result from the binding of target biomolecules to the sensor surface or to interfering effects such as non-specific adsorption of non-target molecules by the sensor surface and background refractive index variations (due to temperature variations, composition fluctuations etc). Hence SPR sensors are dependent on the cumulative effect of refractive index changes in the analyte and also to the surface binding interactions of the biological agent. It is difficult to distinguish the individual effects of analyte refractive index and the surface binding interaction with only one reading. Two channels or two readings are required for the sensor to differentiate between

the bulk index changes and surface binding changes. This concept of using two readings or two channels is known as self referencing. There have been several self referencing methods implemented which will be explained in the next section. The method which we implemented uses two surface plasmon modes and will be described in detail in section 2.1.1.

1.3 Previous work towards self-referencing sensors

Surface binding of a target analyte is known as a specific effect, while changes in refractive index due to changes in analyte concentrations, temperature variations etc. are known as non-specific effects. Self referencing separates specific effects from non-specific effects. This requires a sensor with at least two different outputs. If the sensitivity of the outputs to specific and non-specific effects is different, then the effects can be separated to achieve self-referencing.

Some of these methods used in previous research to create self referencing sensors are described below:

One of the self-referencing schemes being used is a planar light pipe configuration approach [3]. In this approach, the light source is directed on the sensor substrate at two different locations separated by a distance to give rise to two channels. The second channel is functionalized such that the analyte will not bind specifically to the sensor surface and so this channel measures non-specific effects. Surface binding experiments are conducted on the first channel and the second channel is taken as reference.

However a few disadvantages that are noticed in this approach are:

1. Any difference in sensor properties, recognition element surface concentration, or temperature between the two locations could yield errors in the reference measurement.
2. Two separate locations and two separate read outs are required for two channels.

A dual surface plasmon surface sensor approach was suggested by Homola [4] where a thin, high refractive index dielectric overlayer covers part of the substrate to spectrally separate sensing channels. When light is incident on the substrate and overlaps both regions, the reflection spectrum exhibits two dips. The total reflectivity is the sum of composite reflectivities of channel without a dielectric overlayer and channel with dielectric overlayer. The specific response of this dual channel sensor to surface binding interactions is demonstrated by immobilization of biomolecules on one of the channels. It is seen that there is significant change in the spectrum dip of this channel due to surface binding. The other channel showed little response to surface binding. This dual sensor approach is extended to multichannel capability which will allow more sensing channels thereby allowing the sensor to discriminate surface binding from other non specific effects. Some of the disadvantages of this dual sensor approach are
1. Spatial separation of two channels.
2. Reduced signal-to-noise ratio because minimum reflection is ½ for any one channel.
3. Difficult to calibrate because different functionalization chemistries are required for the metal and overlayer.
The separation of surface binding changes from bulk refractive index changes was also demonstrated by Homola et al. in [5] by using a high dielectric oxide overlayer covering a part of metal surface. Polyethyleneoxide (PEO) mixed with biotin terminated thiol, i.e. PEO/BAT thiols are used as self assembled monolayers (SAM) on metal side and PEO silanes served as self

assembled monolayers on metal oxide surface. The concept of self assembled monolayer and its use will be explained in greater detail in the future sections of this work. A solution of streptavidin was introduced on the metal and metal-oxide surfaces and it was seen that metal oxide surface showed very little response to streptavidin solution whereas the metal surface showed high affinity for streptavdin adsorption. It is concluded that the metal oxide accounted for non-specific adsorption and hence it is subtracted from the response of metal surface to extract specific adsorption of streptavidin. This approach followed very complex surface functionalization. This is due to the following reasons.

1. One-step self assembly was not possible as the PEO silanes also react with metal surface leading to inconsistent PEO/BAT SAMs.
2. Cross Contamination is also possible if PEO/BAT thiols react with PEO silanes.

Multichannel capability is described in [6] by Homola et al. A multichannel surface plasmon resonance sensor is demonstrated by first incorporating the dual channel sensor approach (mentioned above) with spectral discrimination of sensing channels by using a dielectric overlayer covering a part of the metal layer. These two channels account for non specific responses of the sensor i.e. refractive index changes due to temperature fluctuations and adsorption of non-target molecules to the sensor surface. Now the sensor is functionalized to have multichannel capability by adding two more channels (one with dielectric overlayer covering a part of metal layer and other with the absence of dielectric overlayer). The response of first two channels is taken as reference to account for non specific response of sensor and the response of other two channels allow the extraction of specific response associated with surface binding.

The self referencing sensor demonstrated here makes use of a prism coupler configuration. This configuration uses a single beam with no dielectric over layer. Also, there is no spatial separation of sensing and reference channels. When light passes through the prism coupler and through the dielectric metal interface it excites two separate surface plasmon modes of the sensor. These two modes exhibit different propagation characteristics and these two modes respond differently to refractive index and surface binding variations. The self referencing aspect of separating the bulk refractive index changes and surface binding changes is thus achieved by exploiting the different sensitivities of the two surface plasmon modes.

Chapter 2

Sensor Theory and Design

2.1.1 Principle of Sensor Operation

A surface plasmon wave or surface plasmon polariton is a TM (Transverse-Magnetic) polarized electromagnetic wave which propagates along the interface between dielectric and metal. So the magnetic vector of the SPR wave is perpendicular to the direction of propagation and parallel to the plane of the interface. The wave vector of a SPR wave propagating along the interface of semi-infinite metal dielectric interface is given by

$$k_{sp} = k_o \sqrt{\frac{\varepsilon_m \varepsilon_d}{\varepsilon_m + \varepsilon_d}}$$

Where k_o denotes the free space wave vector given by $k_o = 2\pi/\lambda$ where λ is the free space wavelength [7]. ε_m denotes dielectric constant of metal and ε_d denotes dielectric constant of dielectric.

Surface plasmon waves exist if the real part of ε_m is less than ε_d, and this condition is satisfied by many metals at optical wavelengths.

The real part of propagation constant determines the phase of the TM wave and imaginary part represents losses occurring in the propagation. The propagation constant of a surface plasmon wave on a thin metal with thickness *h* bounded by two dielectric media (Figure 2.1.1) was determined by Burke et al [8]. The derivation below summarizes their treatment and adopts their notation.

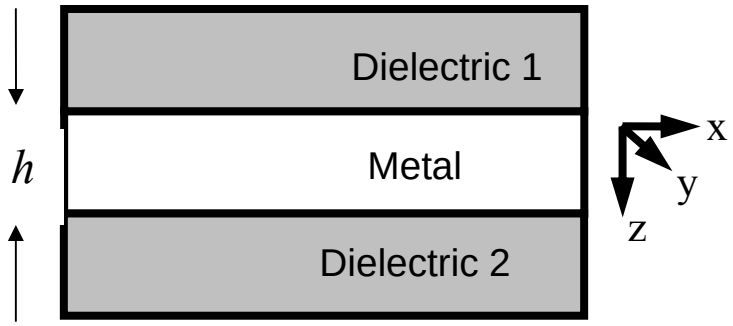

Figure 2.1.1 Dielectric slab surrounding a metal layer of thickness *h*.

For waves propagating along x-axis the magnetic field is oriented in the y-direction and is given by

$$H_y = Cf(z)\exp\left[i(wt-\beta x)\right]$$

where β is the complex propagation constant of SP wave, ω is the frequency, C is normalization constant, and f(z) is a z dependence of magnetic field.

From Maxwell's equations the electric fields can be derived as

$$E_x = \frac{i}{\omega\varepsilon_0\varepsilon}\frac{\partial H_y}{\partial z},\ E_z = -\frac{\beta}{\omega\varepsilon_0\varepsilon}H_y$$

The function f(z) in the three media is given by

$$\varepsilon_1:\ f(z) = \exp\left[S_1 z\right],\ z<0$$

$$\varepsilon_m:\ f(z) = \cosh(S_2 z) + \frac{S_1\varepsilon_m}{S_2\varepsilon_1}\sinh(S_2\varepsilon_1),\ 0<z<h$$

$$\varepsilon_3:\ f(z) = \left[\cosh(S_2 z) + \frac{S_1\varepsilon_m}{S_2\varepsilon_1}\sinh(S_2\varepsilon_1)\right]\exp\left[-S_3(z-h)\right],\ z>h$$

Note that these equations follow Burke et al. closely, but two errors have been corrected in expression for the field profile in the metal.

Where S_1, S_2 and S_3 are given by

$$S_1^2 = \beta^2 - \varepsilon_1 k_o^2,$$

$$S_2^2 = \beta^2 - \varepsilon_m k_o^2,$$

$$S_3^2 = \beta^2 - \varepsilon_3 k_o^2$$

For the continuity of tangential electric field at z=0 and z=h leads to the transcendental equation

$$\tanh(S_2 h)\left(\varepsilon_1 \varepsilon_3 S_2^2 + \varepsilon_2^2 S_1 S_3\right) + \left(S_2\left(\varepsilon_1 S_3 + \varepsilon_3 S_1\right)\varepsilon_2\right) = 0$$

If the slab is symmetric i.e. the refractive index on either side of the metal is identical, it supports two modes which have symmetric and anti-symmetric field profiles [8]. If the slab is asymmetric, it leads to two surface plasmon modes one which is not completely symmetric and one which is not completely anti-symmetric. The two surface plasmon modes are shown in Fig 2.1.2. It can be seen that one of modes extends deeply into the dielectric and the other mode penetrates deeply into the metal film. The mode which exhibits less overlap within the metal and has lower absorption loss is termed the Long Range Surface Plasmon (LRSP) mode. The other mode which exhibits a higher overlap within the metal and hence greater absorption loss is termed the Short Range Surface Plasmon (SRSP) mode. Since the electric field of the short range surface plasmon mode is concentrated at the metal surface, the propagation constant is affected strongly by surface binding. In the same way, the propagation constant of long range surface plasmon mode is affected by the bulk refractive index changes more than the surface binding because it extends more deeply into the solution. This forms the basis of our entire work as we determine to separate the surface binding effects from the bulk refractive index changes using

these two modes based on the fact that the short range mode is more sensitive to surface binding than the long range.

In this work, Teflon AF, an amorphous flouropolymer is used as a buffer layer. It has excellent optical properties and has a refractive index close to water [9]. The thickness of gold film is 55nm. The refractive index of Teflon AF as a function of wavelength was determined by Lowry et al. [9]. The refractive index of Teflon AF at visible and near infrared wavelengths can be determined using a simple Cauchy formula fit. The Cauchy formula states the relation between refractive index and wavelength as

$$n = 1 + A_1 (1 + B_1 / \lambda^2)$$ where A_1 and B_1 are constants [10].

We plotted the refractive index of Teflon AF with wavelength using this Cauchy formula fit in Figure 2.1.3. The refractive index of gold as a function of wavelength is obtained from measurements of variable angle spectroscopic ellipsometer (VASE) measurements done by J.A Woolam Co. These measurements were confirmed using our own gold samples as detailed in Appendix. Also shown in Figure 2.1.4 is the dispersion relation for light incident from a BK7 prism at an angle of 63.9 degrees. It can be seen that the dispersion curves of these two modes intersect with the dispersion curve of prism coupled beam at two distinct points, the long range coupling taking place in visible region and the short range coupling taking place in near infrared region. The curves do not account for any perturbation of the surface plasmon modes by the prism or substrate.

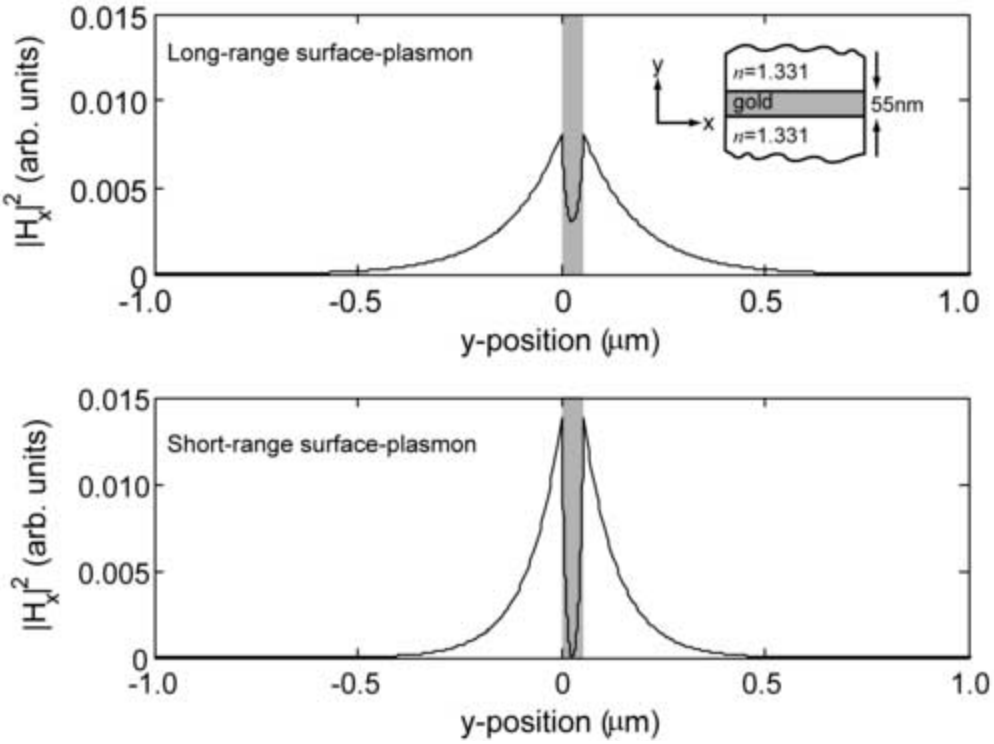

Figure 2.1.2 Calculated magnetic field profiles of the long- and short- range surface plasmon modes supported by a 55 nm thick gold film between dielectrics with refractive index of 1.33. The fields of the long-range (symmetric) mode penetrate deeply into the dielectric allowing for sensitive measurement of background index changes. The fields of the short-range (anti-symmetric) mode are concentrated at the metal surface for better detection of surface binding.

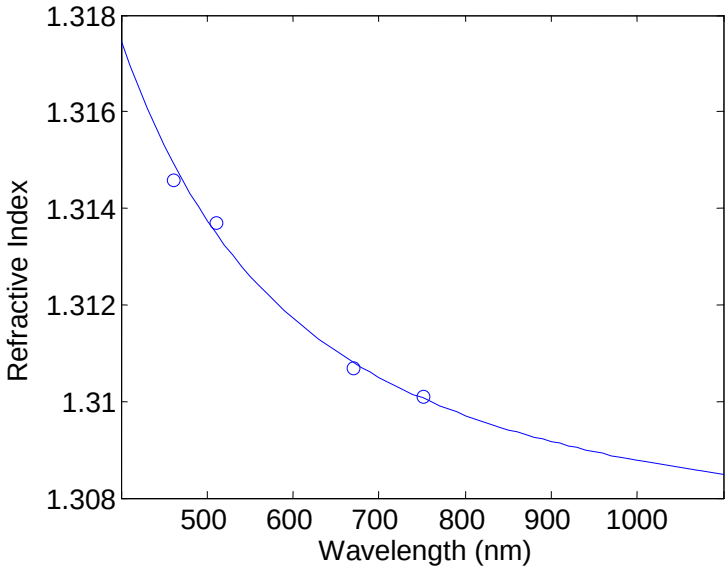

Figure 2.1.3 Refractive index of Teflon AF in the wavelength range of 500-1000nm

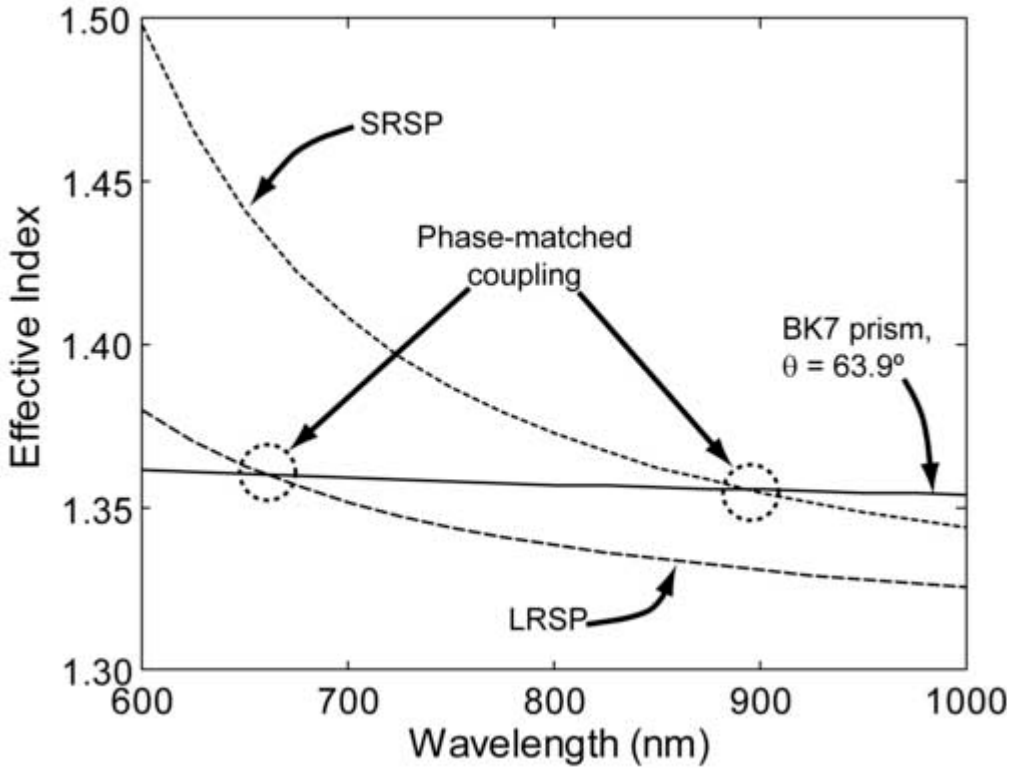

Figure 2.1.4 Calculated dispersion relations for the long-range (LRSP) and short-range (SRSP) surface-plasmon modes of a 55-nm thick gold thin film surrounded by a medium with the refractive index of Teflon-AF. Points of maximum coupling to the surface-plasmon modes are indicated at the intersection of the curves.

2.1.2 Calculating Reflection Spectrum

Fig 2.1.5 shows the prism coupling configuration for our experiment set up. Our goal is to plot the TM reflection spectrum of the sensor and to derive the reflection and transmission coefficients as a function of wavelength.

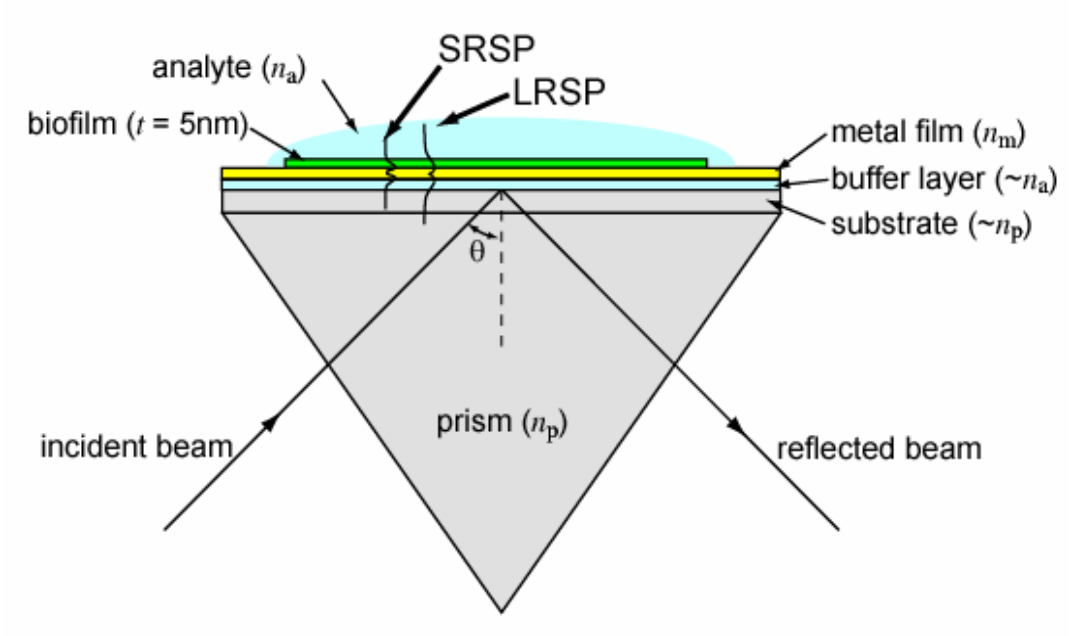

Figure 2.1.5 Prism coupler configuration for simultaneously launching long and short range surface plasmon waves.

When light propagates through different layers, the angles of propagation in these layers are dependent on the refractive indices of these layers. The relation between angle of propagation and refractive index in two media is given by Snell's law

$$\frac{n_1}{n_2} = \frac{\sin(\theta_2)}{\sin(\theta_1)}$$

Where n_1 and n_2 are the refractive indices of medium 1 and medium 2 respectively and θ_1 is the angle of incidence and θ_2 is the angle of propagation at the two media.

For a TM polarized wave, the reflection coefficient is the ratio of reflected magnetic field component parallel to surface and the incident magnetic field parallel to surface. The reflection coefficient is given by

$$r = \frac{n_2 \cos(\theta_1) - n_1 \cos(\theta_2)}{n_2 \cos(\theta_1) + n_1 \cos(\theta 2)}$$

The transmission coefficient is the ratio of transmitted magnetic field component parallel to surface and incident magnetic field parallel to surface.

The transmission coefficient is given by

$$t = \frac{2\ n_1 \cos(\theta_1)}{n_2 \cos(\theta_1) + n_1 \cos(\theta 2)}$$

The power (or intensity) of reflected and transmitted is given by square of the reflection or transmission coefficients.

$$R = |r|^2$$

$$T = |t|^2$$

We used Transmission matrix (T-matrix) theory to calculate the net reflection and transmission for this prism coupling setup. [11]

For the interface between two layers with different refractive indices the T-Matrix is given by

$$T = \begin{bmatrix} 1/t & r/t \\ r/t & 1/t \end{bmatrix}$$

Now, if the wave has to travel a length L in the second layer, the corresponding T-matrix is given by

$$T = \begin{bmatrix} e^{j\beta L} & 0 \\ 0 & e^{-j\beta L} \end{bmatrix}$$

Where β is the propagation constant of the wave inside the layer and L is the distance the wave propagates.

So for a dielectric block of length L the resultant T-Matrix is given by multiplying the individual T-Matrices

$$T = \begin{bmatrix} e^{j\beta L}/t & r/te^{j\beta L} \\ r/te^{-j\beta L} & e^{-j\beta L}/t \end{bmatrix}$$

The main advantage of the T-matrices is that more complicated structures can be modeled simply by matrix multiplying the individual components.

In our case (Figure 2.1.5) light propagates through prism, dielectric buffer layer, metal, adsorbed layer, and finally through the solution. If n_{prism}, n_{buffer}, n_{metal}, n_{layer}, $n_{solution}$ denote the refractive indices of prism, buffer material, metal layer, adsorbed layer and analyte solution and t_{buffer}, t_{metal}, t_{layer} denote the thicknesses of buffer material, metal layer, adsorbed layers, then according to Snell's law the angle of incidence at different points of interaction is calculated as

$$\theta_{01} = \text{asin}(\sin(\theta_0)/ n_{prism})$$

Where θ_0 is the angle of incidence at air-prism interface and θ_{01} is the angle of propagation at air-

prism interface. Since the prism is an equilateral triangle the relation between θ_{01} and θ_1 is given by

$\theta_1 = \theta_{01} + (60/180)\pi = \text{asin}(\sin(\theta_0)/ n_{prism}) + \pi /3$

where θ_1 is the angle of incidence at prism-substrate interface (Figure 2.1.6).

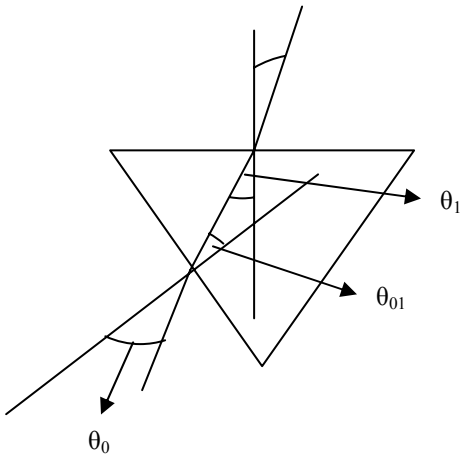

Figure 2.1.6 showing the calculation of angle θ_1 at the prism-substrate interface.

In our case, the refractive index of prism and substrate is same as they are both made up of glass. The angles of incidence at buffer-substrate layer, buffer-metal layer, metal-SAM layer and SAM layer-analyte interfaces are given by

$\theta_2 = \text{asin}(n_{prism}/n_{buffer} \sin(\theta_1))$

$\theta_3 = \text{asin}(n_{buffer}/n_{metal} \sin(\theta_2))$

$\theta_4 = \text{asin}(n_{metal}/n_{layer} \sin(\theta_3))$

$\theta_5 = \text{asin}(n_{layer}/n_{solution} \sin(\theta_4))$

The propagation constants at different layers is calculated as

$k_1 = 2\pi n_{prism}/\lambda \cos(\theta_1)$

$k_2 = 2\pi n_{buffer}/\lambda \cos(\theta_2)$

$k_3 = 2\pi n_{metal}/\lambda \cos(\theta_3)$

$k_4 = 2\pi n_{layer}/\lambda \quad \cos(\theta_4)$

$k_5 = 2\pi n_{solution}/\lambda \cos(\theta_5)$

The net Transmission matrix for the sensor setup is given by the matrix multiplication of individual T-matrices

$$T = [1\ 0]' \times T(n_{solution}, n_{layer}, \theta_4, \theta_5, k_4, t_{layer}) \times T(n_{metal}, n_{layer}, \theta_3, \theta_4, k3, t_{metal}) \times T(n_{metal}, n_{buffer}, \theta_3, \theta_2, k2, t_{buffer}) \times T(n_{prism}, n_{buffer}, \theta_2, \theta_1)$$

Where the components in the parenthesis denote the variables needed to obtain the T-matrix of two layers.

The coefficient of reflection is given by

$$r = T(2)/T(1);$$

The coefficient of transmission is given by

$$t = 1/T(1)$$

Finally the reflectivity (percentage of reflection) can be calculated as

$$R = |r|^2$$

The main performance characteristics of a SPR biosensor are sensitivity and limit of detection.

Sensitivity is the change in sensor output (wavelength, angle of incidence, intensity etc) of the light wave interacting with the SPW wave to either the change in solution index or the concentration of bound analyte on the surface. In our case, we define sensitivity in terms of the change in the resonance wavelength. This sensitivity can be divided into two components, (1) wavelength change due to binding of the analyte to sensor surface and (2) wavelength change due to the effect of change in the solution index. To validate this, we simulated the reflection spectrum of SPR waves. The point where the incident light wave couples to the SP wave can be seen as a dip in the reflection spectrum. In our case we used gold as the metal layer and ethanol as the solution.

Fig 2.1.7 shows reflection spectrum in air showing only one dip in reflection spectrum. Fig 2.1.8 shows reflection spectrum with ethanol for three different thicknesses of gold. It can be seen there are two dips in reflection spectrum showing Long Range and Short Range spectrum with long range peak occurring at lower wavelengths and short range peak occurring at higher wavelengths. Although gold thickness is kept constant in SPR biosensing, it can be seen that the percentage of reflected light for long range and short range SP waves varies with the thickness of gold. Fig 2.1.9 shows reflection spectrum for 2 different scenarios: (1) Ethanol as solution and (2) Changing Ethanol refractive index by 0.001. Figures 2.1.10 and 2.1.11 show the enlarged long range reflection spectrum and enlarged short range reflection spectrum of Figure 2.1.9

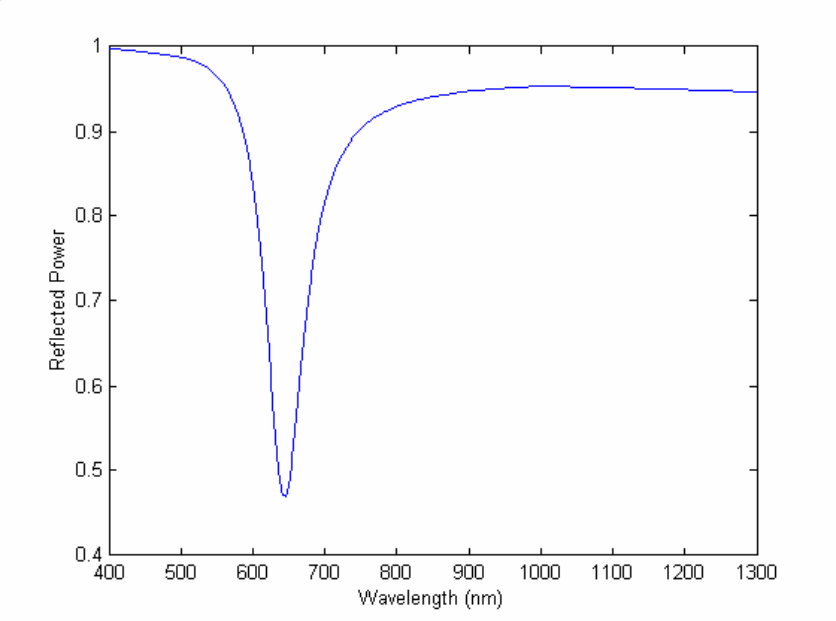

Figure 2.1.7: Reflection spectrum without analyte – BK7+Teflon-AF+Gold stack. Teflon thickness-500nm and gold thickness-60nm.

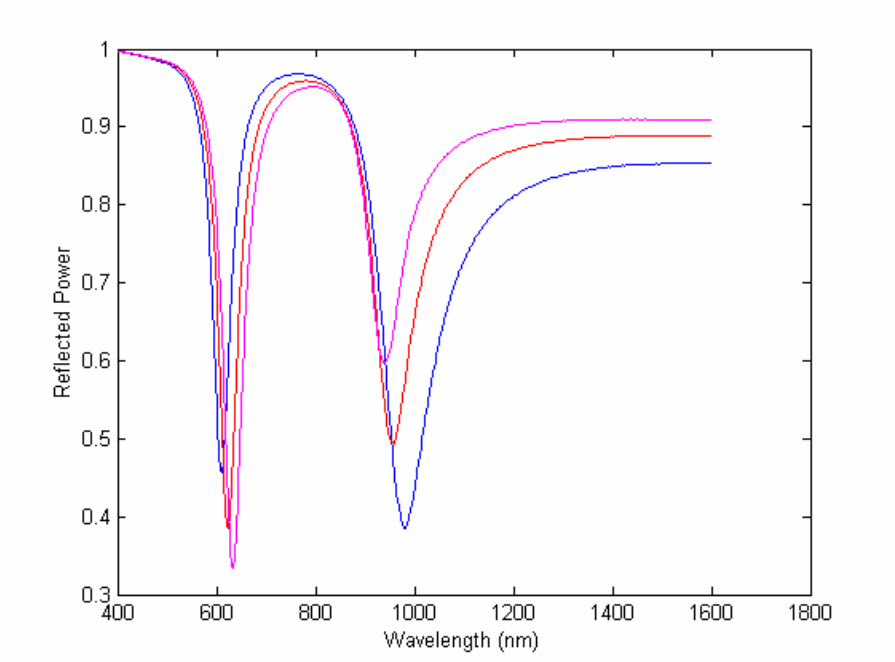

Figure 2.1.8: Reflection spectrum for three different thickness of gold. BK7+Teflon-AF+gold+ethanol stack. Teflon thickness-500nm and three different thickness of Gold- 50nm(blue curve), 55nm(red curve), 60nm(pink curve)

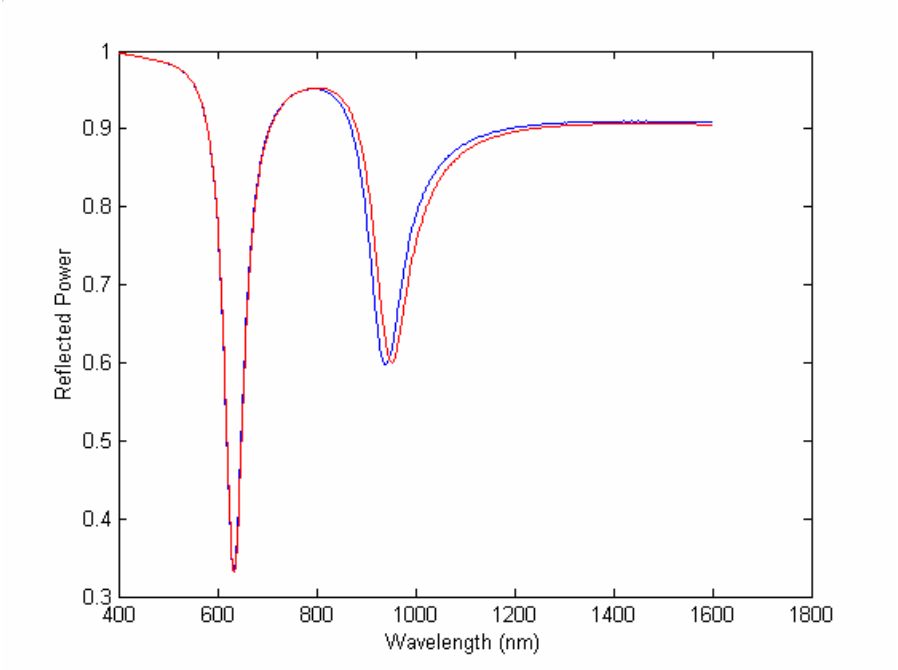

Figure 2.1.9: Reflection spectrum with ethanol solution. Pure ethanol solution(blue curve), Refractive index of ethanol increased by 0.001(red curve).

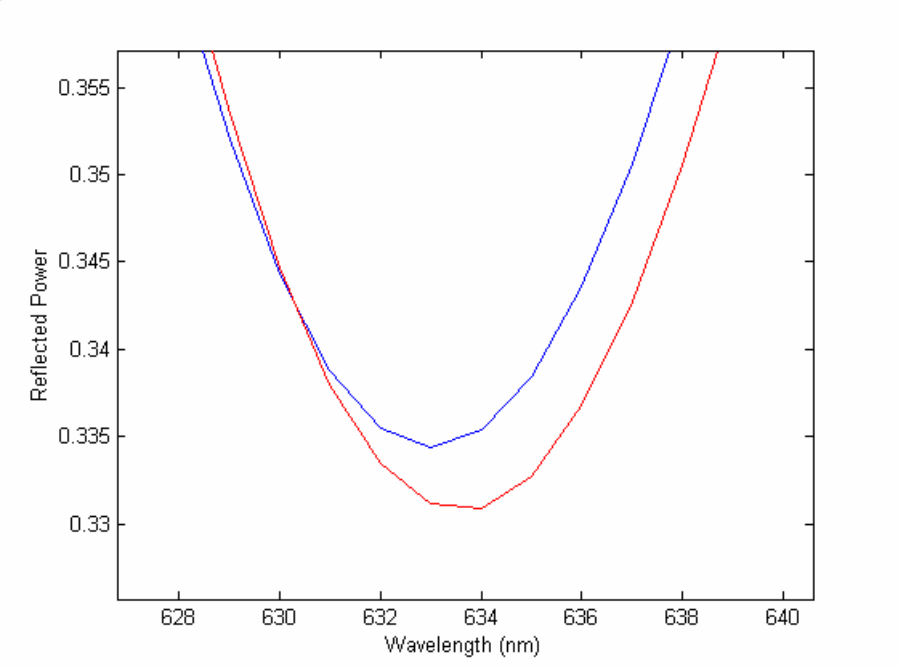

Figure 2.1.10: Enlarged Long Range Reflection spectrum of Figure 2.1.9. Pure ethanol solution(blue curve), Refractive index of ethanol increased by 0.001(red curve).

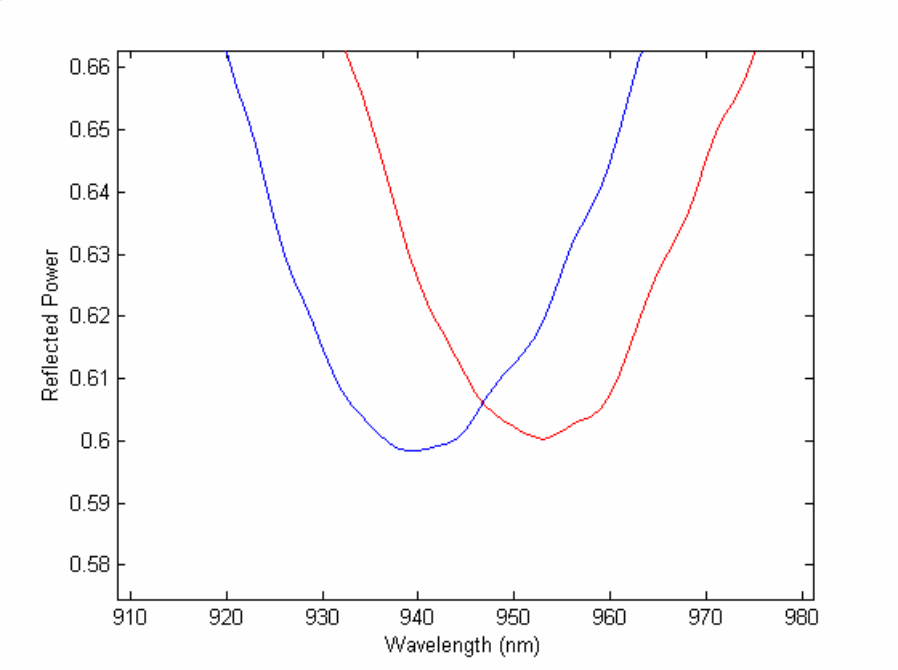

Figure 2.1.11: Enlarged Short Range Reflection spectrum of Figure 2.1.9. Pure ethanol solution(blue curve), Refractive index of ethanol increased by 0.001(red curve).

2.1.3 Sensitivity of Long and Short Range SPW modes

The sensitivities of long and short range surface plasmon modes can be obtained from the reflection spectrum of the sensor. It is to be noted that the Long and Short Range modes have different sensitivities for bulk index changes and surface binding. If the response of long range and short range surface plasmon mode follows linearly with the surface binding changes and bulk refractive index changes, then the long range and short range surface plasmon resonance shifts, $\Delta\lambda_{LR}$ and $\Delta\lambda_{SR}$ are given by

$$\Delta\lambda_{\text{LR}} = S_{\text{S-LR}}\Delta t + S_{\text{B-LR}}\Delta n_B, \text{ and}$$

$$\Delta\lambda_{\text{SR}} = S_{\text{S-SR}}\Delta t + S_{\text{B-SR}}\Delta n_B$$

Where $S_{S\text{-}LR}$ and $S_{S\text{-}SR}$ are the surface binding sensitivities and $S_{B\text{-}LR}$ and $S_{B\text{-}SR}$ are the bulk refractive index sensitivities of long and short range modes respectively. Δt and Δn_B are the

adsorbed layer thickness change and bulk refractive index change respectively.

If the Sensitivities are known, the bulk index change (Δn_B) and surface layer thickness change (Δt) can be calculated as

$$\Delta t = \frac{\Delta\lambda_{\text{LR}} / S_{\text{B-LR}} - \Delta\lambda_{\text{SR}} / S_{\text{B-SR}}}{S_{\text{S-LR}} / S_{\text{B-LR}} - S_{\text{S-SR}} / S_{\text{B-SR}}}, \text{ and}$$

$$\Delta n_{\text{B}} = \frac{\Delta\lambda_{\text{LR}} / S_{\text{S-LR}} - \Delta\lambda_{\text{SR}} / S_{\text{S-SR}}}{S_{\text{B-LR}} / S_{\text{S-LR}} - S_{\text{B-SR}} / S_{\text{S-SR}}}.$$

Because we measure two resonance shifts to estimate Δt and Δn_B, predicting limits of detection is slightly more involved than for a standard SPR sensor. If we assume the measurement noise for $\Delta\lambda_{\text{LR}}$ and $\Delta\lambda_{\text{SR}}$ is not correlated, then we can simply add the variances of the terms in the numerators of above mentioned equations. The resulting limits of detection (LOD) at three standard deviations are given by

$$\text{LOD}\left(\Delta t\right) = 3 \text{ sqrt}\left[\frac{\text{var}\left(\Delta\lambda_{\text{LR}}\right)/S_{\text{B-LR}}^2 + \text{var}\left(\Delta\lambda_{\text{SR}}\right)/S_{\text{B-SR}}^2}{\left(S_{\text{S-LR}} / S_{\text{B-LR}} - S_{\text{S-SR}} / S_{\text{B-SR}}\right)^2}\right]$$

$$\text{LOD}\left(\Delta n_{\text{B}}\right) = 3 \text{ sqrt}\left[\frac{\text{var}\left(\Delta\lambda_{\text{LR}}\right)/S_{\text{S-LR}}^2 + \text{var}\left(\Delta\lambda_{\text{SR}}\right)/S_{\text{S-SR}}^2}{\left(S_{\text{B-LR}} / S_{\text{S-LR}} - S_{\text{B-SR}} / S_{\text{S-SR}}\right)^2}\right]$$

It should also be noted that the dependence of the resonance wavelengths on the product of the bound layer and the background index changes can be significant. In such case the long range and short range surface plasmon resonance shifts are given by

$$\Delta\lambda_{\text{LR}} = S_{\text{S-LR}}\Delta t + S_{\text{B-LR}}\Delta n_B + S_{\text{SB-LR}}\Delta t\Delta n_B, \text{ and}$$

$$\Delta\lambda_{SR} = S_{S\text{-}SR}\Delta t + S_{B\text{-}SR}\Delta n_B + S_{SB\text{-}SR}\Delta t\Delta n_B$$

Where $S_{SB\text{-}LR}$ and $S_{SB\text{-}SR}$ describe product dependence of long and short range resonances respectively. Although, one must numerically solve this complex set of nonlinear equations to determine Δt and Δn_B from measurements of $\Delta\lambda_{LR}$ and $\Delta\lambda_{SR}$, there will be an improved accuracy in the measurements by including this product term.

2.2 Selection of Materials and Refractive Indices

The next step is to determine the materials that make up the sensor. In our experiments Teflon is used as buffer cladding layer, Gold as Metal layer, Ethanol as main solution. This section describes few reasons for selecting these materials.

Reason for using Teflon AF:

The Teflon AF materials have the lowest commercially available index of refraction. Also, they are extremely resistant to chemical attack and exhibit low moisture absorption. The transmission of Teflon in the wavelength range of our interest from 500-1000nm is shown in Figure 2.1.3.

The primary reason for using Teflon is that refractive indices of different solutions used in our experiments such as ethanol, methanol and water match very closely with the refractive index of Teflon. This aspect is very important for realization of sensor as self-referencing sensor. In addition, Teflon's chemical stability allows simple integration into bio-chemical sensors.

Reason for using Gold:

Gold supports surface-plasmon waves in the visible and near infrared regions. In addition, gold is very stable and not reactive with the chemical used. Gold is the most extensively used metal in fabricating SPR sensors.

Reason for using Ethanol:

Ethanol serves as a solvent for the octadecanethiol molecules that will form a self-assembled monolayer on the gold surface. The refractive index of ethanol also closely matches with that of the Teflon buffer layer, so both SR and LR plasmon waves can be excited. A few other reasons are its low cost, its low toxicity, its low tendency to be incorporated into the self assembled monolayers and its availability in high purity.

2.3 Initial Sensor Design

Any sensor design consists of identifying the materials that are used for the sensor. In our experiments we used a BK7 prism which is approximately 25.4mm thick. As outlined above, Teflon is used as the base cladding layer and it is spin coated to a thickness of 500nm+-10%. This is because we found out that we get a good working area for a range of wavelengths where the sensor can couple to long range and short range modes. Again as outlined above, gold is the metal layer used and its thickness is in the range of 50-60 nm. In this range we found out that the reflection spectral dips are very narrow for short and long range modes. When higher thicknesses of Gold are used the sensor doesn't couple to short range modes (red color curve in Fig 2.3.1), the reason being the short range modes can not penetrate through the thick layers of gold. When lower thicknesses of gold are used the sensor doesn't couple to long range modes or the short

range modes (pink color curve in Fig 2.3.1), within the range of visible to near IR wavelengths that can be measured with a silicon detector. In addition, the prism more strongly perturbs the long-range mode in this case. So in our case, we found a very good working area for Teflon thickness in the range of 500-600nm and gold thickness in the range of 50-60nm. The blue color curve in Fig 2.3.1 shows the reflection spectrum for a gold thickness of 50nm. It can be seen that the incident light excites both long range and short range modes. Ethanol is the main solution used in our experiments. We ensured that proper care is taken to maintain clean conditions all throughout the fabrication process.

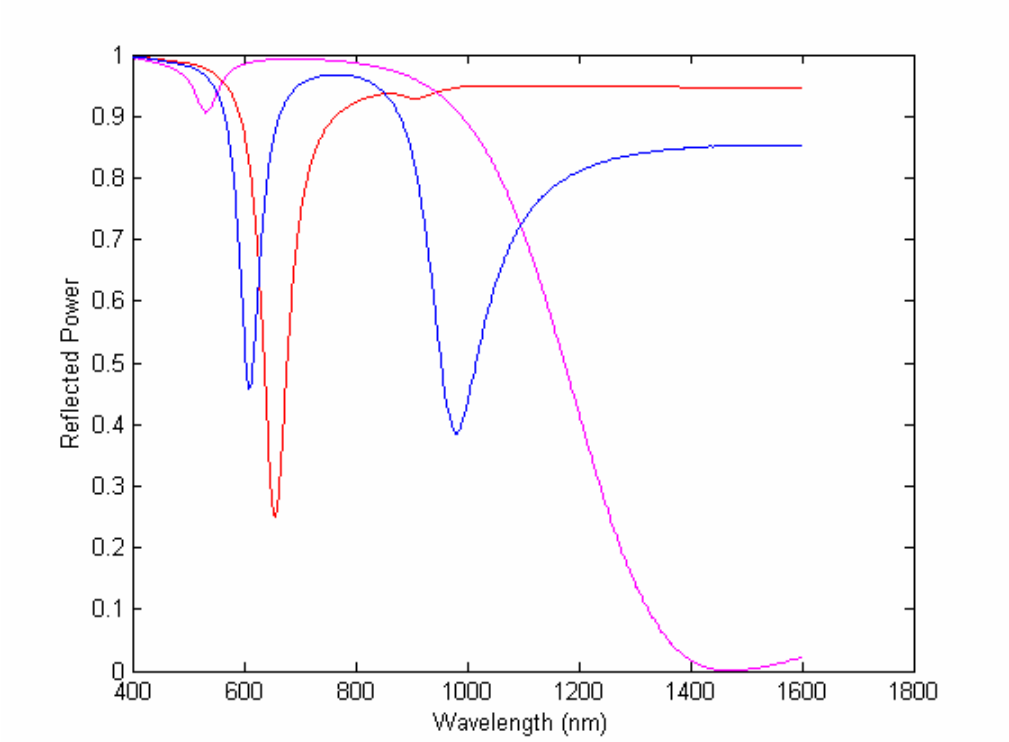

Figure 2.3.1: Reflection spectrum for three different thickness of gold. BK7+Teflon-AF+gold+ethanol stack. Teflon thickness-500nm and for three different thickness of Gold. 50nm(blue curve), 100nm(red curve), 32nm(pink curve)

Chapter 3

Sensor Fabrication

3.1 Spin coating of Teflon

To begin the sensor fabrication process the BK7 substrate is first cleaned with isopropyl alcohol and acetone and blown dry with nitrogen.

1. Preparation of Teflon solution: The Teflon AF-1600 solution is mixed with FC-40 Fluorinert solvent in the ratio of 2:1 by volume. Both Teflon AF-1600 solution and FC-40 solvent are obtained from Dupont Inc. 40ml of Teflon AF-1600 solution is mixed with 20ml of FC-40 solvent and the solution is stirred with a magnetic stirrer for about 15-20 minutes. The stirrer is cleaned with isopropyl alcohol and DI water before its use. The roughness of the spin coated Teflon layer was 5nm approximately. Initially when Teflon was used with FC-77 solvent the roughness was measured to be 50nm. So there was approximately 90% reduction in the roughness of Teflon layer when FC-40 was used as the solvent. The next step is to spin coat this Teflon solution on BK7 substrate.

2. An adhesion promoter is spin coated prior to spin coating Teflon to improve the adhesion of Teflon to the substrate. The adhesion promoter used is 1H, 1H, 2H, 2H perfluorodecyltriethoxy silane (Lancaster Synthesis, Inc.). Adhesion promoter solution is made by mixing 2% of adhesion promoter with 95% ethyl alcohol and 2% water. This adhesion promoter is spin coated at 1000RPM. After this, the sample is baked at 112C for 10mins. This is done to evaporate any residual solvent.

3. The Teflon solution is next spin coated at a speed of 1000RPM and then the sample is baked at 112C for 10mins. After this the sample is baked again at 180C for 5mins. This combination produced a thickness of 1.5microns. The spin speed is varied to produce desired thickness of Teflon. A spin speed of 2000RPM produced 1.2micron thick Teflon layer. The thickness of Teflon layer we wanted to achieve is 500nm, we found out that a spin speed of 3000RPM gives us desired thickness of 500nm for Teflon layer.

3.2 Deposition of Gold

Gold is deposited on the Teflon layer using electron beam evaporation. The e-beam evaporator is shown in the Figure 3.2.1. Gold deposited is obtained from Kurt Lesker, Inc which is 99.9% pure. A minimum pressure of 2.0×10^{-6} is used as the starting point before gold deposition and a voltage of 8kv is maintained throughout the evaporation. The thickness of gold in our experiments is in between 50-60nm.

Figure 3.2.1 Electron-beam evaporator (University of Kentucky)

3.3 Measurement of layer thicknesses

Thickness of Teflon:

We used an ellipsometer to measure the thickness of Teflon layer. The ellipsometer is operated at 633nm wavelength and provides three different angles of incidence on the substrate. Since BK7 is only weakly reflective, we spin coated the Teflon layer on a silicon substrate simultaneously, maintaining the same spin speeds and processing conditions as that of the BK7 sample. The Teflon layer thickness is measured with the ellipsometer. The thickness is also confirmed with stylus profiler at various positions. This is done by scratching the Teflon layer on silicon substrate. The thickness measured by stylus profiler is approximately 10% higher than that measured by the ellipsometer. It should be noted the real thickness of Teflon layer on sensor might be few nanometers off from the thickness of Teflon layer on silicon.

Thickness of Gold:

The same procedure is used for measuring gold thickness i.e. by taking a silicon sample and evaporating gold on the silicon substrate. This sample and the sensor are coated with gold in the e-beam evaporator at the same time. This ensures that gold is deposited on these two samples at identical thickness. Again, the ellipsometer is used to measure thickness of gold on silicon substrate, because of the non-reflecting nature of BK7 substrate. This ellipsometer comes with software which takes the readings for an angle of incidence and gives the thickness and refractive index of layer of interest as output. Appendix section describes how we determined the refractive index of gold.

Chapter 4

Experimental Section

4.1 Experimental Setup

Figure 4.1.1 shows the schematic diagram of surface plasmon resonance sensor used in our setup.

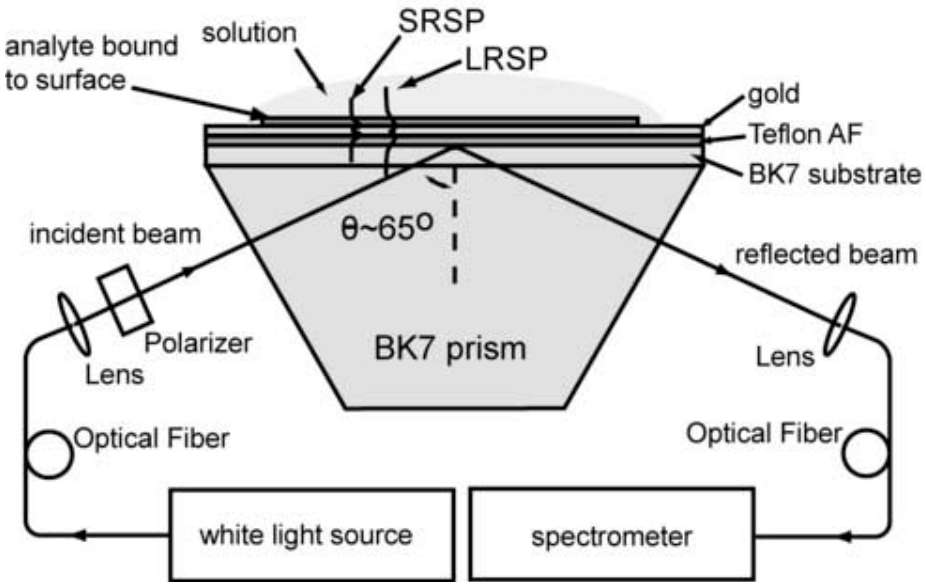

Figure 4.1.1 Schematic diagram of a self-referencing surface-plasmon resonance sensor. The sensor consists of a thin gold film on a buffer layer that is closely matched to the solution in interest.

The sensor substrate is placed in contact with a BK7 equilateral prism (Esco Products, Inc.) using a BK7 specific index matching fluid (Cargille, Inc.). The prism and sensor are clamped in a custom made ultra-high molecular weight polyethylene (UHMW) flow cell sealed with either a neoprene or polytetrafluoroethylene (PTFE) gasket. Liquids are introduced to the sensor surface through PTFE tubing using a vacuum pump and liquid trap. The trap consists of a 500mL side-arm Erlenmeyer flask maintained at 17 kPa using a rotary vacuum pump and a bleed valve. A

polyetheretherketone (PEEK) micro-metering valve (Upchurch Scientific) is used to control the liquid flow rate.

The flow-cell/sensor assembly is mounted on a custom designed variable angle optical reflection measurement system. Light from a halogen lamp (Model DH-2000, Ocean Optics, Inc.) is introduced into the reflection measurement apparatus using a 200 μm core multi-mode optical fiber. A collimating lens directs the light from the fiber through a calcite Glan-Taylor polarizer (ThorLabs, Inc.) and into the prism. The polarizer is mounted in a rotation stage that can be adjusted such that either a TE or TM wave is incident on the sensor. The reflected light is collected by another lens and coupled to a multimode fiber which routes it to a computer controlled spectrometer (Ocean Optics model HR-4000). The figure 4.1.2 shows the snapshot of sensor setup

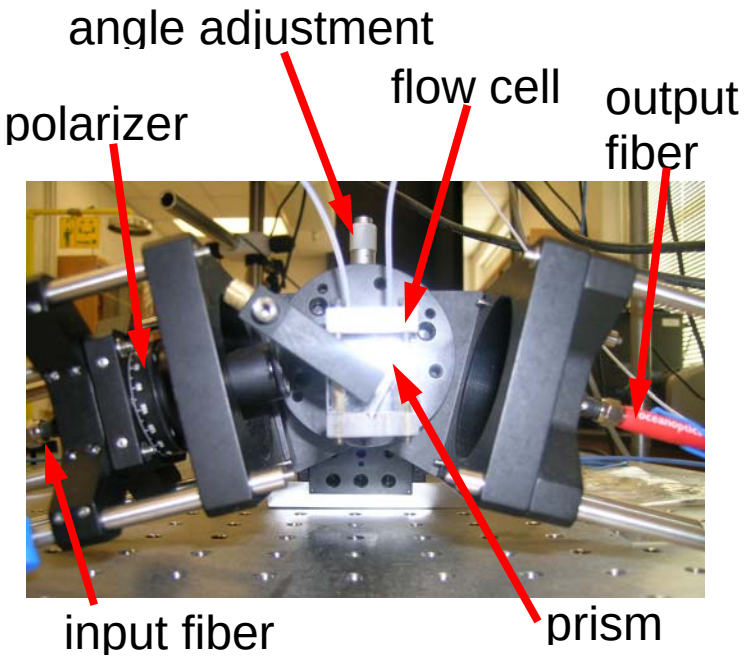

Figure 4.1.2 Picture of the optical system with major component labeled.

Introduction of Self Assembled Monolayers:

A self assembled monolayer is a layer one molecule thick that can covalently bind to the surface. A very good example is the reaction of alkanethiols with gold [12]. Another example of self assembled monolayers is the reaction of silanes with glass [13]. Some of the potential applications of self assembled monolayers are in the areas of lubrication, corrosion protection, photolithographical or electrical resists, and sensing [12]. In our work, octadecanethiol (ODT) is used as the SAM layer.

Reason for using octadecanethiol as monolayer:

Octadecanethiol monolayers form as a uniform single molecule thick layer. ODT has a single sulphur atom which binds very strongly to gold and this process is essentially irreversible. ODT is a large hydrocarbon molecule (18 carbon atoms) which yields a relatively thick (~2 nm) surface layer.

It was seen that octadecanethiol layer reaches a thickness of 2nm in 4.3 minute incubation time [14] and this value was taken as the standard for the thickness of octadecanethiol in all our experiments. We also tried to measure the thickness of ODT layer on gold using ellipsometer. Although we were not able to derive the exact thickness from ellipsometer readings, we were able to determine that the values were different compared to the gold layer without the ODT layer.

4.2 Description of Experiment

The TE reflection spectrum is taken as reference for all measurements. Once the spectrum is

referenced, the polarizer is rotated to TM (90 degrees shift) to view the functioning of the sensor. The reflection spectrum can be viewed using Ocean Optics software. We also designed Labview software to plot the peak wavelengths of the spectrum in real time.

The outline of our experiment is as follows:

1. Initially when there is no ethanol solution flowing through the flow cell, there is no coupling of surface plasmon waves.
2. When ethanol is flowed through the cell, long and short range surface plasmon resonances appear, as seen in Figure 4.2.1. The output of Labview software plots these long and short range peak wavelengths as a function of time. Even though there is some disturbance that can be noticed when ethanol is initially flowed, the output becomes steady after sometime (less than a minute).
3. After the spectrum become steady, the flow stream is switched to a solution containing 95% ethanol and 5% methanol. There is a momentary loss of surface plasmon waves soon after this switch occurs, but it is difficult to notice. This is due to the formation of bubbles in the flow cell during this switch. The short and long range peaks shift to shorter wavelengths Figure 4.2.2. This is due to the effective refractive index decrease as a result of dilution of ethanol concentration with methanol.
4. Once again after the spectrum becomes steady, the flow steam is switched to a solution containing 90% ethanol and 10% methanol. The short and long range peaks shift to still shorter wavelengths Figure 4.2.2. It can be noticed that the sensitivity is positive in these regions. After this, the solution is reverted back to ethanol. The long and short range waves return to the same wavelengths as before with the ethanol solution.

5. This is the main step in the whole experiment where octadecanethiol is introduced. So the flow stream is switched to octadecanethiol solution so that the octadecanthiol binds to gold surface resulting in the formation of monolayer. As the ODT layer starts binding to the gold surface there will be a gradual increase in the surface coverage of monolayer and because of this there is a gradual increase in the peak wavelengths of long and short range SP waves Fig 4.2.2, step4. As a concession to ellisometric characterization of SAMs in the literature, we represent fractional coverage in terms of average thickness. After the spectrum becomes steady (5 minutes) the thickness of monolayer is approximated to be 2nm.

6. The flow stream is switched back to ethanol solution. The peak wavelengths for long and short range modes shift to higher wavelengths as compared to the peaks when the sensor is without the monolayer.

This is the critical point in our work as the output spectrum proves that the sensor is sensitive to surface binding.

7. The flow stream is switched to 95% ethanol and 5% methanol solution and 90% ethanol and 10 % methanol solutions the only difference being this time the ODT layer is bound to surface. The sensor works as expected as can be seen in Figure 4.2.2.

9. In the end, ethanol is flowed through the sensor and the experiment is ended. The spectrum comes back to the original position as in Figure 4.2.2.

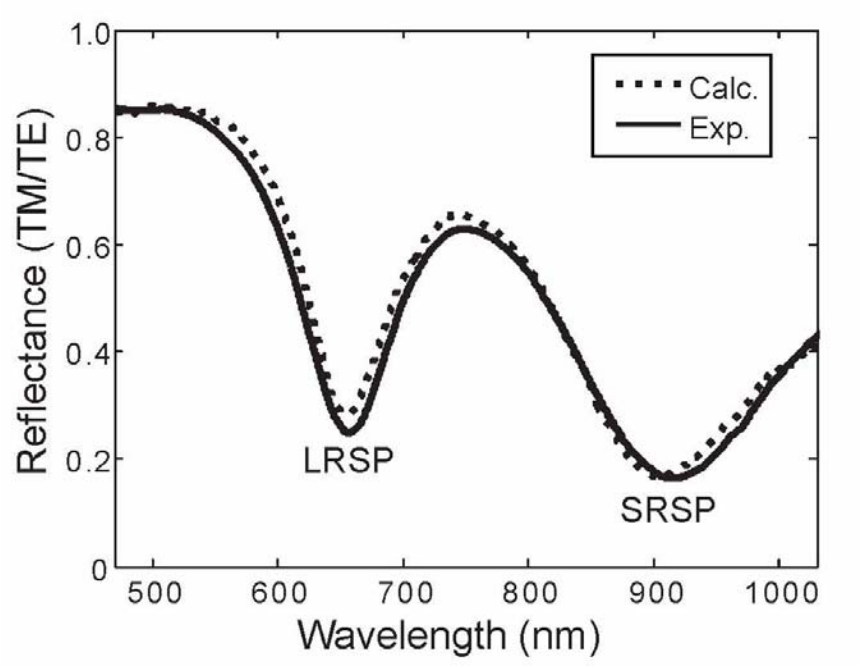

Figure 4.2.1 Experimental reflection spectrum showing coupling to both long range and short range surface plasmon modes.

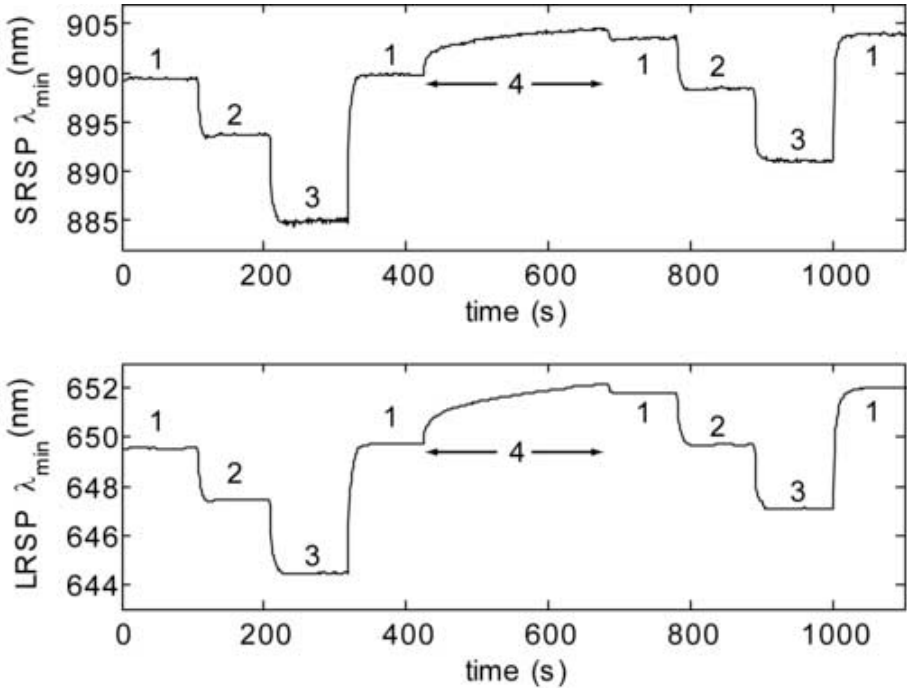

Figure 4.2.2 Top-Plot of long range resonance wavelength with time. Bottom-Plot of short range resonance wavelength with time.

Precautions for the future:

1. The sensor setup should be fairly undisturbed during the whole experiment. Even slight movements can vary the flow rate of the solution and the angle of incidence.
2. Making sure that the flow tube is immersed completely in the beakers thus preventing any unwanted bubbles.
3. It is suggested that the experiment room contains as minimal external light interacting with the sensor as possible.
4. All the solutions used must be maintained at room temperature in our case, as temperature has effect on refractive index of the solution.
5. Transferring the flow cell between different solutions must be done quickly to avoid bubbles in the flow cell.

4.3 Experimental Results

Experiment 1: The first experiment sought to measure the sensors response to varying solution refractive indices. This is demonstrated by mixing water with ethylene glycol solution. The Figure 4.3.1 shows the sensor response (experiment) when ethylene glycol is mixed with water. The blue curve is when there is no solution flowing through the sensor. The red curve shows the reflection when pure water is flowing through the sensor. After sometime, a solution containing 40ml water and 2ml ethylene glycol is introduced through the sensor (pink curve in Figure 4.3.1) and soon after that a solution containing 40ml water and 4ml ethylene glycol (black curve in Figure 4.3.1) is flowed through the sensor.

From Figure 4.3.1, it can be observed that the peaks of long and short range modes shift to higher wavelengths because of increase in refractive index of water-ethylene glycol mixtures.

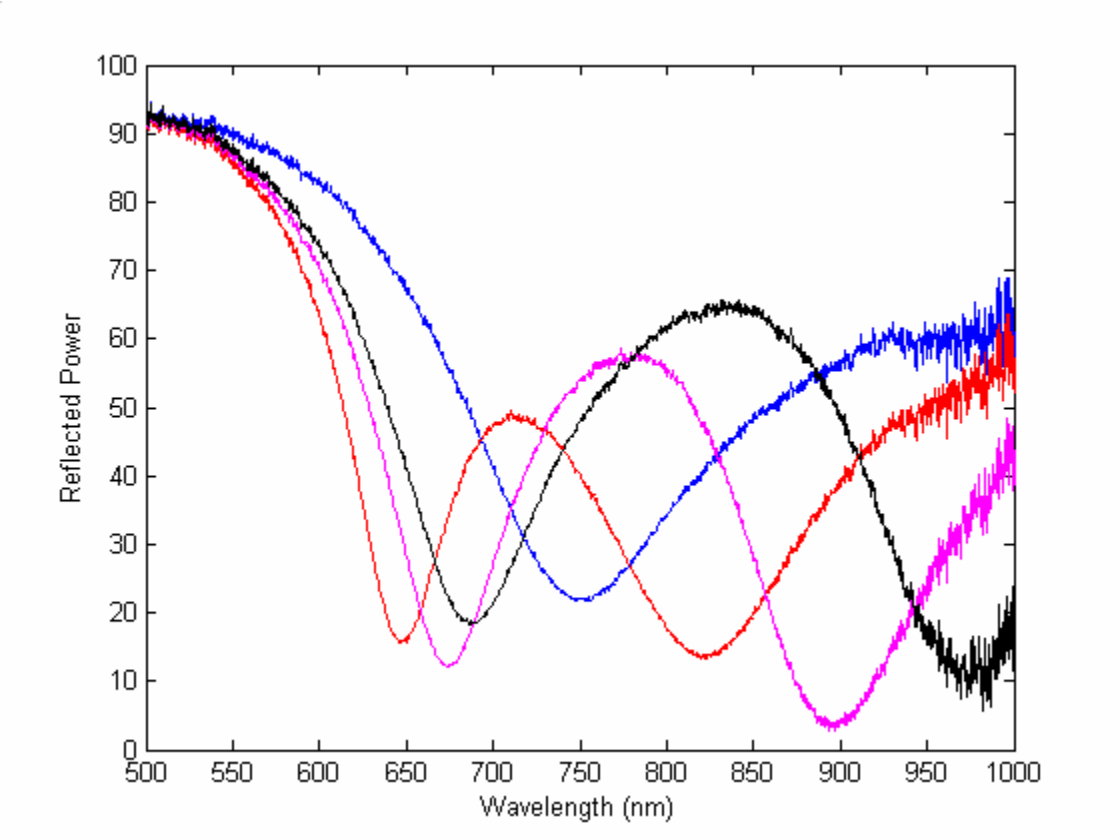

Figure 4.3.1: Sensor response (experiment) to refractive index change by adding ethylene glycol to water

Experiment 2: In this experiment we demonstrated that the temperature of the solution changes the refractive index of the solution and the sensor responds to these refractive index changes. We used water to demonstrate this and the reflection spectrum can be seen in figure 4.3.2.

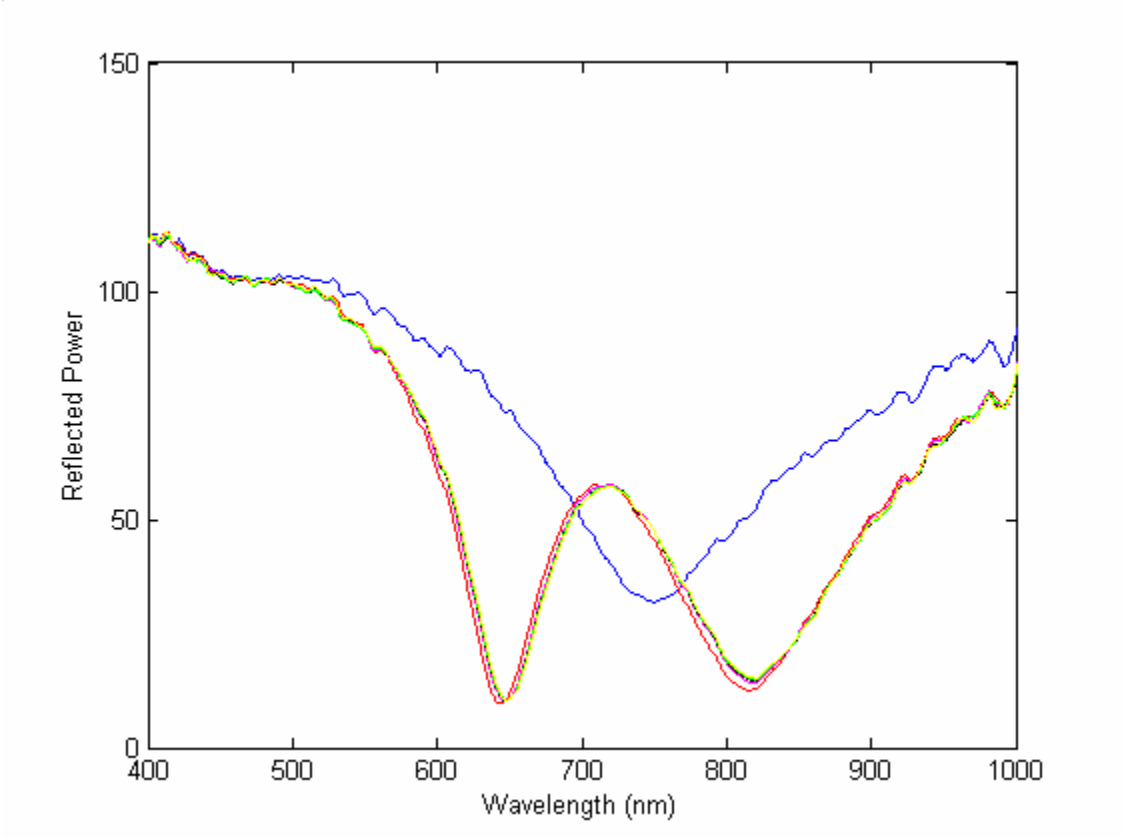

Figure 4.3.2 Reflection spectrum at different temperatures of water. Blue curve shows the reflection spectrum when there is no solution present.

Water at 80C is passed through the sensor and the peaks are measured.

As this water cools down, the subsequent peaks are measured after 1, 2, 3 and 5 minutes. As water gradually cools down with time, the refractive index of water also changes. The refractive index of water increases as the temperature of water decreases in the range between 80-20C. The refractive index of water increases by 0.00988 as it cools down from 80-20C. From the figure it can be seen the curves do not drift apart too much, as the refractive index change of water with temperature is very small (Figure 4.3.2). Figure 4.3.3 and 4.3.4 shows the enlarged reflection spectrum of Fig 4.3.2 for long range peaks and short range peaks. In the case of both long and short range SP waves, the peaks occur at higher wavelengths as water cools down.

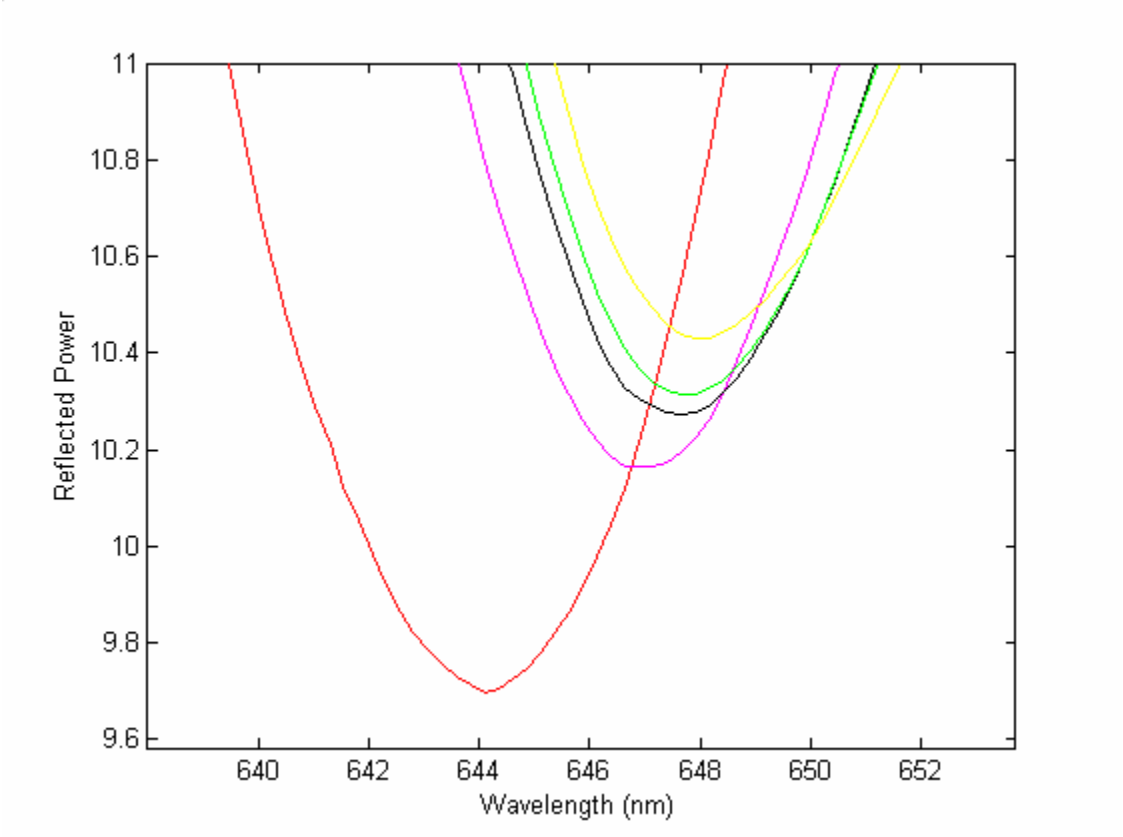

Figure 4.3.3: Long range mode response to temperature of water. water at 80C(red curve), After 1 minute of cooling down of water(pink curve), After 2 minutes of cooling down of water(black curve), After 3 minutes of cooling down of water(green curve), After 5 minutes of cooling down of water(yellow curve).

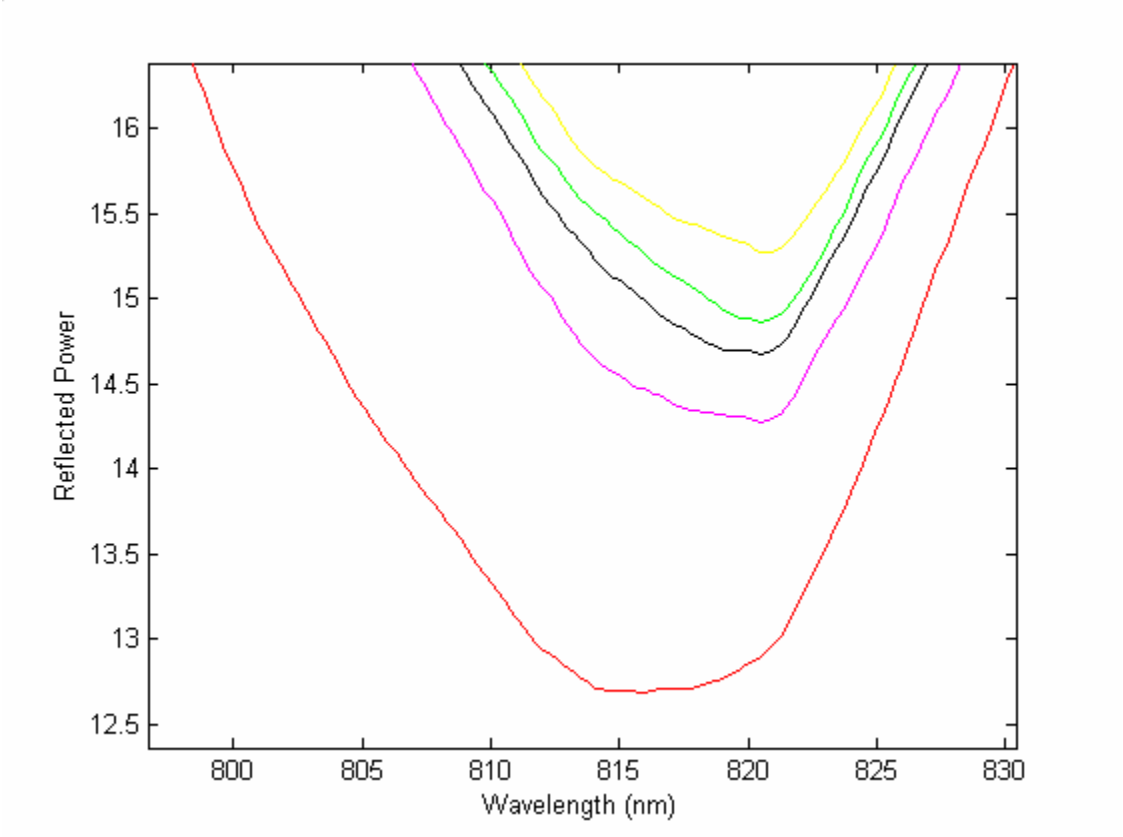

Figure 4.3.4: Short range mode response to temperature of water. water at 80C(red curve), After 1 minute of cooling down of water(pink curve), After 2 minutes of cooling down of water(black curve), After 3 minutes of cooling down of water(green curve), After 5 minutes of cooling down of water(yellow curve).

Main Experiment:

In this section we compare the experiment and simulation results for the main experiment. The long range and short range peaks for experiment and simulation are shown in Table 4.3.1 and Table 4.3.2 respectively. The experimental results are obtained from Figure 4.2.2. For simulation we used the following values: angle of incidence of 67 degrees, Teflon thickness of 500nm and gold thickness of 60nm, ODT thickness of 2nm after 4.3 min incubation time [14], refractive index of Teflon[9], refractive index of gold[J.A. Woolam Co.'s measurements, as supplied with their VASE ellipsometer], refractive index of ODT[14] and refractive index of ethanol-methanol mixtures[15].

Comparison of long range resonance peaks between experiment and simulation:

Peak Resonance wavelength	Experiment(nm)	Simulation(nm)
100% Ethanol without SAM	649.5	633
95% Ethanol+5% Methanol without SAM	648	632
90% Ethanol+10% Methanol without SAM	644.5	631
100% Ethanol with SAM	651.5	634
95% Ethanol+5% Methanol with SAM	650	633
90% Ethanol+10% Methanol with SAM	648	632

Table 4.3.1 Long Range mode peaks from experiment and simulation

Comparison of short range resonance peaks between experiment and simulation:

Peak Resonance wavelength	Experiment(nm)	Simulation(nm)
100% Ethanol without SAM	900	939
95% Ethanol+5% Methanol without SAM	894	919
90% Ethanol+10% Methanol without SAM	884	903
100% Ethanol with SAM	903	959
95% Ethanol+5% Methanol with SAM	898	938
90% Ethanol+10% Methanol with SAM	892	922

Table 4.3.2 Short Range mode peaks from experiment and simulation

For Long Range and Short Range SP waves, there is a maximum of 6.5% offset between experimental results and simulation.

Reasons that might explain this offset include

1. Angle of incidence is not determined accurately. Even a 0.001 degree error in the angle measured can make a significant difference.
2. The thickness of gold is not determined accurately.
3. We observed a change in thickness of Teflon after evaporation of gold.

Figure 4.3.5 shows the reflection spectrum from simulation and Figures 4.3.6 and 4.3.7 show the enlarged reflection spectrum of Figure 4.3.5 for Long Range peaks and Short Range peaks.

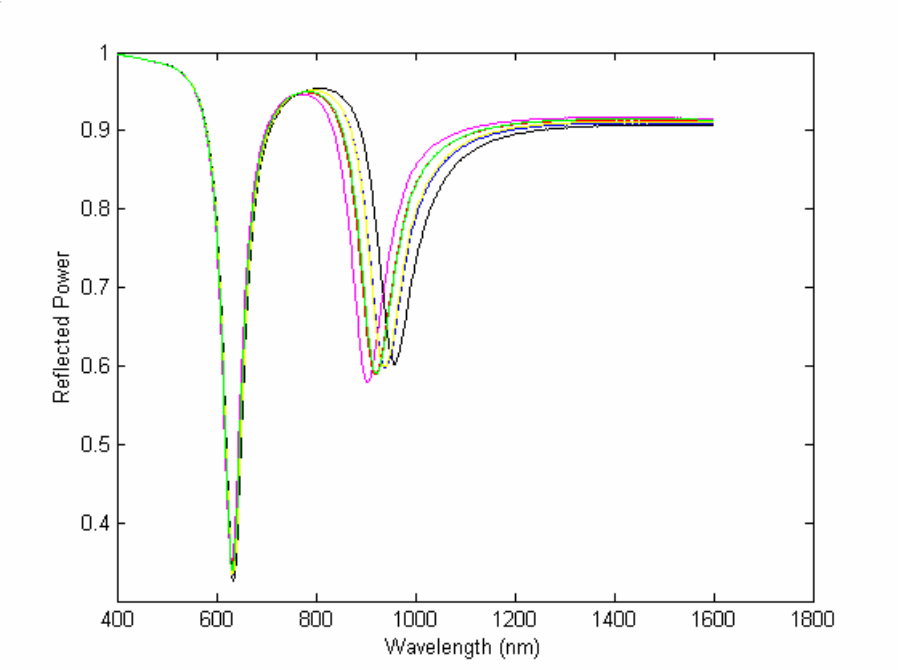

Figure 4.3.5 – Reflection spectrum from simulation BK7+Teflon-AF+Gold+ODT+varying concentration of Ethanol. Teflon thickness-500nm, gold thickness-60nm, ODT thickness-2nm. Blue curve - 100% ethanol without ODT, red curve – 95% ethanol+5% methanol without ODT, pink curve 90% ethanol+10% methanol without ODT, black curve – 100% ethanol with ODT, yellow curve – 95% ethanol+5% methanol with ODT, green curve 90% ethanol+10% methanol with ODT.

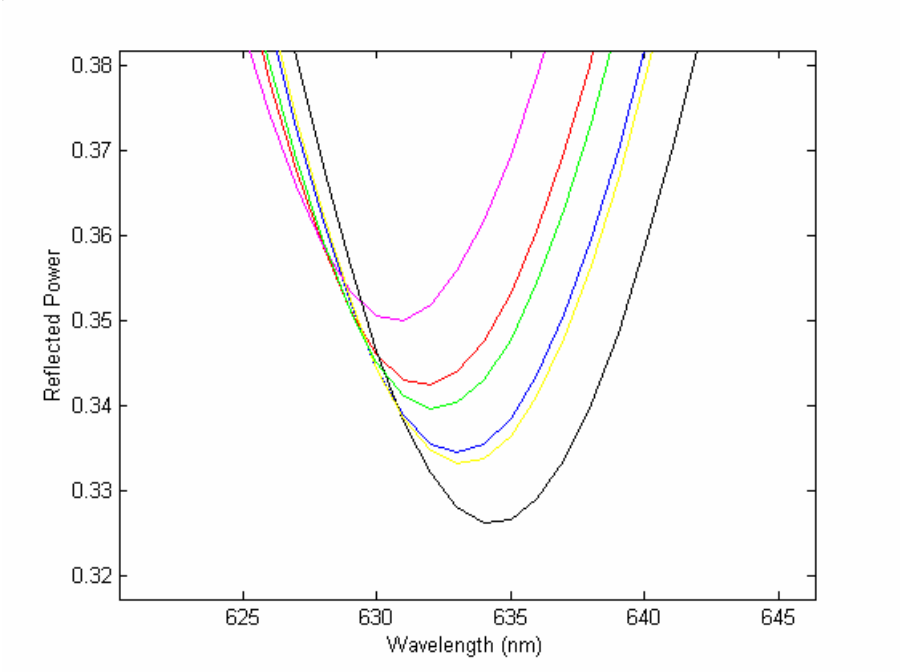

Figure 4.3.6 Enlarged Long Range Reflection spectrum of Figure 4.3.5. Blue curve - 100% ethanol without ODT, red curve – 95% ethanol+5% methanol without ODT, pink curve 90% ethanol+10% methanol without ODT, black curve – 100% ethanol with ODT, yellow curve – 95% ethanol+5% methanol with ODT, green curve 90% ethanol+10% methanol with ODT.

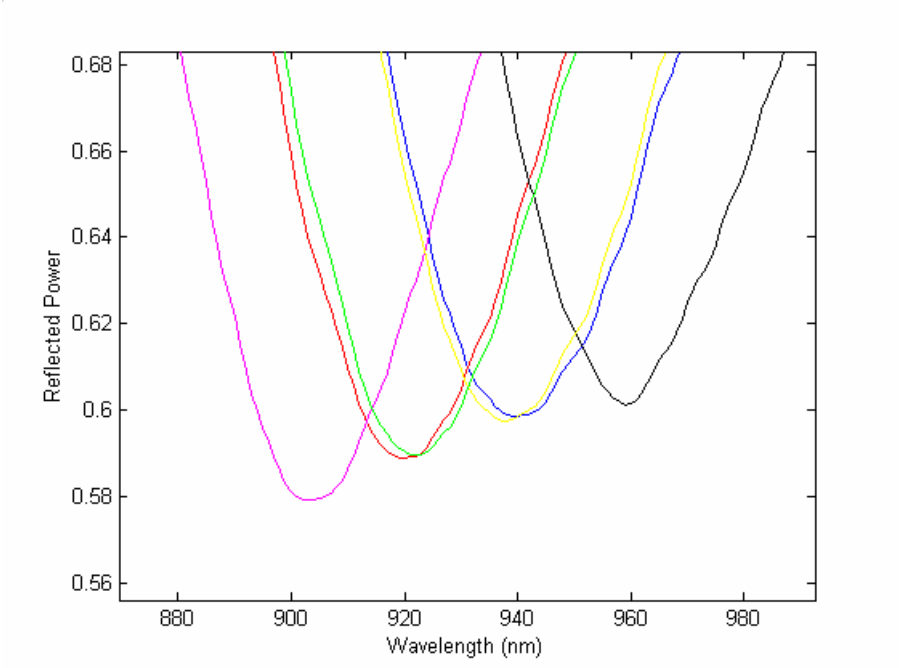

Figure 4.3.7 Enlarged Short Range Reflection spectrum of Figure 4.3.5. Blue curve - 100% ethanol without ODT, red curve – 95% ethanol+5% methanol without ODT, pink curve 90% ethanol+10% methanol without ODT, black curve – 100% ethanol with ODT, yellow curve – 95% ethanol+5% methanol with ODT, green curve 90% ethanol+10% methanol with ODT.

4.4 Analysis and Discussion

From the output spectrum the following points can be observed.

1. The sensitivity of long range and short range modes is positive in the wavelength range observed.

2. The long and short range modes respond differently to bulk index and surface binding variations.

3. The sensor is stable for at least tens of minutes at a time.

4. Even though noise is part of any spectrum output, it is found to be very minimal here.

6. Also, the SPR sensor is highly sensitive to bulk refractive index changes and surface binding changes.

The sensitivities of long range and short range modes for surface layer thickness change and bulk refractive index change are calculated by numerically solving the linear equations in section 2.1.3 for Δt and Δn_B. We determined the refractive index change to be 0.00133 between pure ethanol and 5% methanol in ethanol [15]. Because the sensor performs more linearly over this small index range, we choose this as our calibration point, rather than the 10% methanol in ethanol. The data of Whitesides et al. suggests that the ODT monolayer thickness will be 2.0 nm after the 4.3 minute incubation time is adopted here [14]. Thus, we choose this bulk refractive index change and surface-layer thickness change as our calibration points.

The bulk index sensitivities for LRSP and SRSP for the linear model are found to be 1600nm/RIU and 4100nm/RIU respectively. It can be seen that the sensitivity of short range mode to bulk index change is higher than that of long range mode. This is attributed to more

closely matched dispersion relations of the short range surface plasmon and the incident light in the prism coupler.

The surface-binding sensitivities for LRSP and SRSP are 1.1nm/nm-thickness and 2.2nm/nm-thickness respectively. It can be seen that the higher sensitivity of short range mode is again attributed to more closely matched dispersion relations and enhanced surface field strength. The difference in sensitivities further ensures the effectiveness of the self-referencing scheme.

We also compared the sensitivities of bulk refractive index changes and surface binding changes for experiment and simulation. The theoretical sensitivity values are derived from the values obtained from simulated reflection spectrum Figure 4.3.5. It can be seen that the initially calculated theoretical values are significantly different from the

Sensitivities	Bulk(nm/RIU)		Surface(nm/nm)	
	SR	LR	SR	LR
Experimental	4900	1600	2.2	1.1
Theoretical	15000	752	1.5	0.5
Theoretical(corrected)	3900	1900	1.7	1.2

Table 4.4.1: Comparison of sensitivities for bulk refractive index changes and surface binding changes

experimental values. The reasons for this offset are explained in the previous section. We corrected these theoretical values by curve fitting the reflection spectrum of Figure 4.2.1 to determine the angle of incidence, thickness of Teflon and gold. We found the values to be

68.4 degrees, 350nm and 46nm for angle of incidence, thickness of Teflon and gold respectively. The theoretical corrected sensitivities are shown in Table 4.4.1 and we find a considerably closer match with experimental sensitivities for bulk refractive index and surface binding changes.

While surface and bulk sensitivities for the linear model provide points of comparison for other sensors, modeling a nonlinear sensor response provides more effective self-referencing. Specifically, we account for the sensor's response to the product of film thickness and background refractive index change as incorporated in section 2.1.3. The sensitivity parameters for both the linear and nonlinear models are summarized in Table 4.4.2. It can be seen that the sensitivity values for linear model are the same as the experiment sensitivity values in Table 4.4.1.

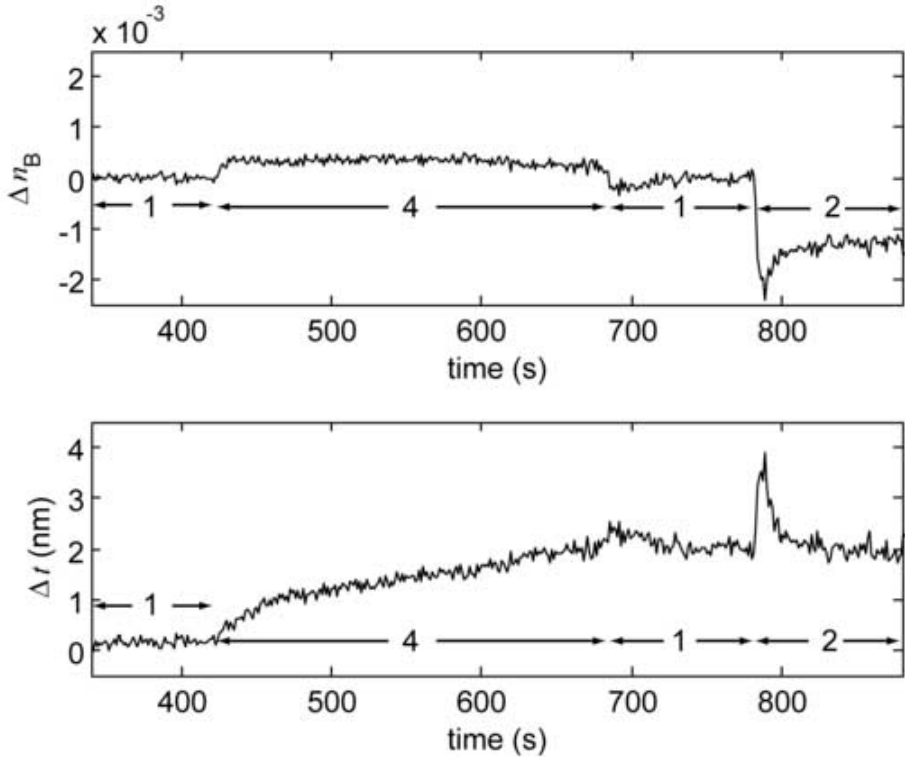

Figure 4.4.1 plots the solution index and average surface layer thickness as a function of time during monolayer formation. The labeled regions indicated the solution flowing and correspond to those in Fig. 4.2.2: (1) EtOH, (2) 95% EtOH + 5% MeOH, and (4) 3.2 mM octadecanethiol (ODT) in EtOH. Note that the self-referencing sensor can distinguish the change in surface-layer thickness from the change in background refractive index due to the presence of ODT or methanol in solution.

The solution index and surface layer thickness are simultaneously determined by numerically solving the nonlinear set of equation in section 2.1.3 for Δt and Δn_B. Fig. 4.4.1 plots the solution index and average surface layer thickness as a function of time during monolayer formation. It can be observed that the solution index measurement is not largely affected by the gradual increase in monolayer thickness. In addition, the measured surface layer thickness is largely unaffected by the solution index change due to the presence of either ODT or methanol in solution. So our self-referencing scheme performs as expected. We observe slight deviations in the thickness measurement when the solutions are switched. This is because of the non-linear response to solution index that is not fully accounted by the six coefficient model presented above.

Although we have yet to optimize the self-referencing sensor design, it is helpful to investigate the limits of detection for both surface-layer thickness changes and for solution index changes. We find LODs at 3-standard deviations of the baseline response of an equilibrated sensor. The baseline measurement of pure ethanol indicates the LOD for solution index to be 4.6×10^{-5} RIU at 100msec per sample. Assuming uncorrelated noise, this translates to a LOD of 1.4×10^{-5} RIU for a standard 1 sec sample time. The surface-layer LOD is estimated as 0.21 nm for 100msec sampling and 0.065 nm for standard 1 sec sampling. Because the sensor is noise limited LOD would improve with increased optical power, with better coupling efficiency, and with reduced spectrometer noise.

Linear Model			Nonlinear Model			
Mode	Sb(nm/RIU)	Ss(nm/RIU)	Mode	Sb(nm/RIU)	Ss(nm/RIU)	Ssb(nm/nm.RIU)
LRSP	1600	1.1	LRSP	1600	1.1	0.037
SRSP	4100	2.2	SRSP	4300	2.0	-181

Table 4.4.2 Sensitive parameters of long range and short range modes for bulk refractive index and surface binding changes from linear and non-linear model

Chapter 5

Conclusions and Future Work

A self-referencing surface plasmon resonance sensor was demonstrated using a structure that supports both short and long range surface plasmon modes. Simultaneous excitation of both short and long range modes is advantageous because

1. No dielectric overlayer is required to separate sensing and reference channels.
2. In other self referencing schemes two separate read-outs are required for sensing and reference channels, whereas here just one read-out is sufficient.
3. The sensor is straightforward to fabricate and the fabrication process is very repeatable.
4. The reflection spectrum of this sensor is consistent with the dimensions of sensor parameters such as thickness of gold, thickness of Teflon layer etc, for example whenever the sensor is fabricated with a thicker gold layer, we observed that the long range mode peaks in the reflection spectrum shift to higher wavelengths and the short range mode peaks in the reflection spectrum shift to lower wavelengths and vice-versa.

We conclude that the self referencing sensor presented in this work can be used to distinguish bulk refractive index changes and surface binding interactions. We have demonstrated this self referencing capability by exciting long and short range surface plasmon modes and by binding octadecanthiol to the gold layer from an ethanol solution.

Suggestions for Future Work:

1. Future work can be based on fabricating self referencing sensor that are optimized for higher sensitivities. The thicknesses of gold and Teflon can be varied for optimal performance and the

experiments can performed with various analytes.

2. One of the most challenging steps we encountered in the whole process is to estimate the thickness of Teflon AF layers and gold layers. This problem is further compounded by the erroneous readings of gold thickness on the crystal monitor of e-beam evaporator. Accurate and precise determination of the thickness of Gold and Teflon layers can be done by taking the sensor to a place where there is proper equipment to measure the thicknesses.

3. Different self assembled monolayers can be used in our experiments and their surface binding phenomenon can be studied.

4. The variable angle spectrometer that is used is not precise enough to determine the angle of incidence. This is very important in simulations as the sensor is very sensitive to the angle of incidence to a degree of 0.001.

The self referencing scheme presented above can be taken as basis and further progress can be made by using complex analytes or by binding various self assembled monolayers to gold. Even though the goal might not be to determine the absolute values i.e. to determine the exact thickness of binding layer but instead it can be used to see how the sensor response differs when studying the surface binding of different monolayers on gold.

Appendix

Determination of Refractive Index of Gold

To determine the refractive index of gold we used a Variable-Angle Spectroscopic Ellipsometer (VASE J.A. Woolam Inc.) at the University of Louisville. This value is again confirmed with our single angle, single wavelength ellipsometer readings. We used a 2 layer stack on silicon substrate with PMMA as the second layer and gold which is used in the sensor is deposited on the top of PMMA layer. We prepared three different samples having three different thickness of gold. The VASE ellipsometer can emit light in the range of wavelengths from 300-1000nm and the real and imaginary part of refractive index of gold is plotted for three different angles of incidence using VASE software. These reading are compared with our Gartner ellipsometer readings for these 3 samples at a wavelength of 632.8nm and the compared values for these 3 samples are shown in tables A1, A2, A3 respectively.

10nm Sample	VASE ellipsometer	UK Gartner ellipsometer
Real part of refractive index(n)	0.1880	0.1880
Imaginary part of refractive index(k)	-3.5681	-3.5668
Thickness of gold(d in nm)	20.019	19.632

Table A1 Shows comparison for 10nm sample

20nm Sample	VASE ellipsometer	UK Gartner ellipsometer
Real part of refractive index(n)	0.1882	0.1827
Imaginary part of refractive index(k)	-3.4569	-3.4673
Thickness of gold(d in nm)	32.357	32.834

Table A2 Shows comparison for 20nm sample

30nm Sample	VASE ellipsometer	UK Gartner ellipsometer
Real part of refractive index(n)	0.1788	0.1770
Imaginary part of refractive index(k)	-3.3931	-3.3596
Thickness of gold(d in nm)	34.049	35.568

Table A3 Shows comparison for 30nm sample

The graphs of *n* (real part of refractive index of gold) & *k* (real part of refractive index of gold) from VASE ellipsometer for wavelength range between 300nm – 1000nm for 10nm sample, 20nm sample and 30nm sample are shown in Figures A1, A2, A3 respectively. The 3 different green curves represent experimental readings for 30, 50, 70 degrees angle of incidence and the red curve represent the generated readings by VASE ellipsometer software.

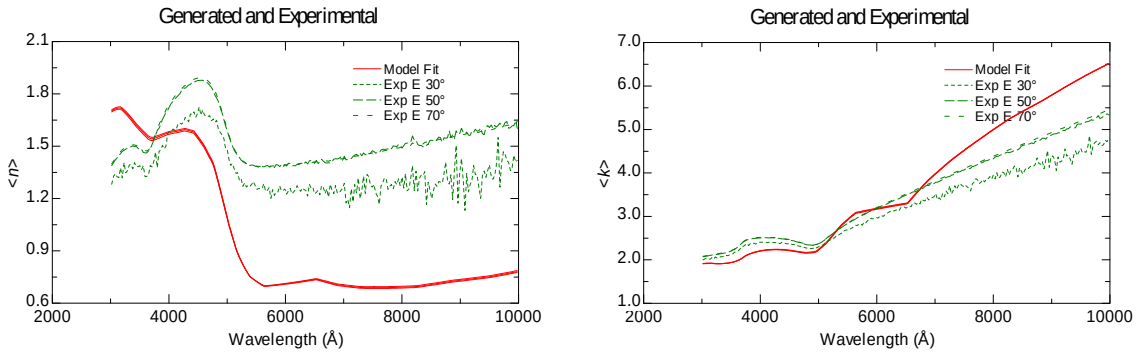

Figure A1 Left figure shows real part of refractive index(n) and right figure shows imaginary part of refractive index(k) for 10nm sample.

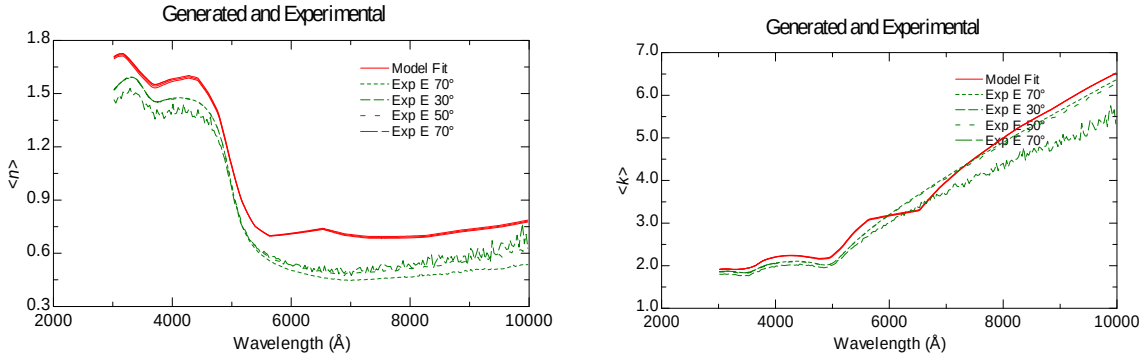

Figure A2 Left figure shows real part of refractive index(n) and right figure shows imaginary part of refractive index(k) for 20nm sample.

For 30nm target gold thickness sample:

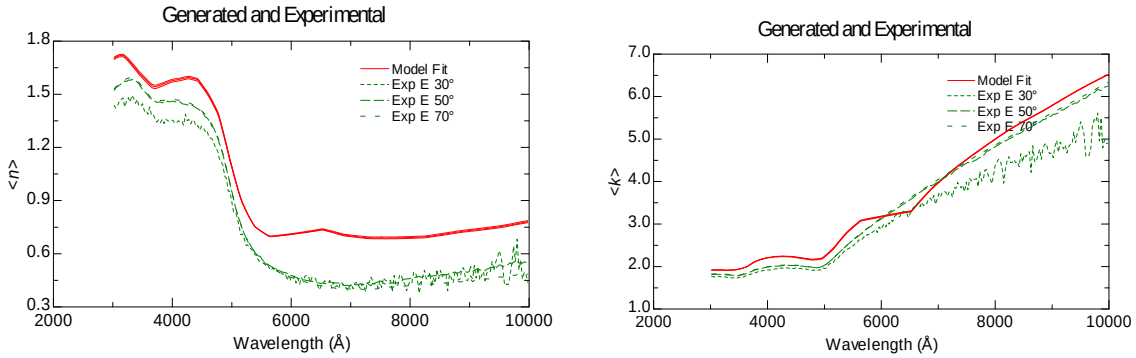

Figure A3 Left figure2 shows real part of refractive index(n) and right figure shows imaginary part of refractive index(k) for 30nm sample.

REFERENCES

[1] J. Homola, Present and future of surface plasmon resonance biosensors, Analytical and Bioanalytical Chemistry 377 (2003) 528-539.

[2] E.N. Economou, Surface Plasmons in Thin Films, Physical Review 182 (1969) 539-554.

[3] G.G. Nenninger, J.B. Clendenning, C.E. Furlong, S.S. Yee, Reference-compensated biosensing using a dual-channel surface plasmon resonance sensor system based on a planar lightpipe configuration, Sensors and Actuators B: Chemical 51 (1998) 38-45.

[4] J. Homola, H.B. Lu, S.S. Yee, Dual-channel surface plasmon resonance sensor with spectral discrimination of sensing channels using dielectric overlayer, Electronics Letters 35 (1999) 1105-1106.

[5] C. Boozer, Q.M. Yu, S.F. Chen, C.Y. Lee, J. Homola, S.S. Yee, S.Y. Jiang, Surface functionalization for self-referencing surface plasmon resonance (SPR) biosensors by multi-step self-assembly, Sensors and Actuators B-Chemical 90 (2003) 22-30.

[6] J. Homola, H.B. Lu, G.G. Nenninger, J. Dostalek, S.S. Yee, A novel multichannel surface plasmon resonance biosensor, Sensors and Actuators B: Chemical 76 (2001) 403-410.

[7] Reather H (1983) Surface plasmons on smooth and rough surfaces and on gratings, Springer

[8] J.J. Burke, G.I. Stegeman, T. Tamir, Surface-Polariton-Like Waves Guided by Thin, Lossy Metal-Films, Physical Review B 33 (1986) 5186-5201.

[9] J.H. Lowry, J.S. Mendlowitz, N.S. Subramanian, Optical Characteristics of Teflon AF Fluoroplastic Materials, Optical Engineering 31 (1992) 1982-1985.

[10] Born, M. and Wolf, E. Principles of Optics: Electromagnetic Theory of Propagation,

Interference and Diffraction of Light, 7th ed. Cambridge, England: Cambridge University Press, 1999.

[11] Lasers and Photonic Integrated Circuits by Larry A.Coldren ,Scott W.Corzine.

[12] Sensor Functionalities in Self-Assembled Monolayers by Simon Flink, Frank C. J. M. van Veggel and David N. Reinhoudt Adv. Mater. 2000, 12, No. 18, September 15

[13] J. Sagiv, J. Am. Chem. Soc. 1980, 102, 92.

[14] C.D. Bain, E.B. Troughton, Y.T. Tao, J. Evall, G.M. Whitesides, R.G. Nuzzo, Formation of Monolayer Films by the Spontaneous Assembly of Organic Thiols from Solution onto Gold, Journal of the American Chemical Society 111 (1989) 321-335.

[15] L. Albuquerque, C. Ventura, R. Goncalves, Refractive indices, densities, and excess properties for binary mixtures containing methanol, ethanol, 1,2-ethanediol, and 2-methoxyethanol, Journal of Chemical and Engineering Data 41 (1996) 685-688.

[16] J. T. Hastings.; R. K. Donipudi.; V. de Silva., Self-referencing SPR Sensors using both Long- and Short-Range Surface-Plasmons submitted to *Sensors and Actuators B – Chemical* 2006.

VITA

The author was born in Anantapur, Andhra Pradesh, India on December 17, 1981. In 2003, he completed his under graduation in India at Chaitanya Bharathi Institute of Technology, in the Department of Electrical Engineering. In August 2003 he was awarded Kentucky Graduate Scholarship and joined University Of Kentucky to pursue his MS in Electrical Engineering. During the course of the program, he worked in the Department of Electrical Engineering as a Research Assistant at Centre for Nanoscale Science and Engineering (CeNSE).